DEVELOPMENT OF A PROCESS PARAMETER SELECTION GUIDELINE FOR ADDITIVELY MANUFACTURING NEW MATERIALS VIA LASER POWDER BED FUSION

A Thesis

by

HANNAH MARY BOON

Submitted to the Office of Graduate and Professional Studies of
Texas A&M University
In partial fulfillment of the requirements for the degree of

MASTER OF SCIENCE

Chair of Committee,	Ibrahim Karaman
Co-Chair of Committee,	Alaa Elwany
Committee Member,	Raymundo Arroyave
Head of Department,	Ibrahim Karaman

May 2019

Major Subject: Materials Science and Engineering

ABSTRACT

As new materials are designed for metal additive manufacturing (AM), there is a need to develop a systematic approach to optimize process parameters. The purpose of this research is to develop a guideline for laser-based powder bed fusion (LPBF) operators that will minimize computational and experimental trial and error. The guideline illustrates a two-step optimization problem based on the following four process parameters: laser power, scan speed, layer thickness, and hatch distance. The first step focuses on optimizing laser power and scan speed parameters in order to achieve desirable melt pool dimensions. The Eagar-Tsai model was employed as an aid to predict the width and depth of the melt pool. The second step optimizes the latter two parameters by considering the melt pool geometry from step one and calculating the optimal hatch distance while mitigating lack of fusion. Characterization of single tracks and cubes is performed to explore the relationship between process parameters and porosity and differential evaporation of a binary nickel alloy.

DEDICATION

To my wonderful mother.
Thank you for your love, support and encouragement
over the years.

CONTRIBUTORS AND FUNDING SOURCES

Contributors

This work was supervised by a thesis committee consisting of Dr. Karaman, advisor, chair of committee and Department Head in the Department of Materials Science and Engineering, Dr. Elwany, co-chair of committee in the Department of Industrial and Systems Engineering, and Dr. Arroyave, committee member in the Department of Materials Science and Engineering. Early work was also supervised by Dr. Ma, post-doc in the Department of Materials Science and Engineering.

The design of experiments for the first and second round single track experiments was conducted in part by Bing Zhang, graduate student in the Department of Industrial and Systems Engineering. The characterization of the second round of single tracks was conducted by Raiyan Seede, graduate student in the Department of Materials Science and Engineering. All other work conducted for the thesis was completed independently by the student.

Funding Sources

This work was made possible in part by the Air Force Research Laboratory and by a College of Engineering Fellowship from Texas A&M University.

NOMENCLATURE

Symbol or Acronym	*Description*
AM	Additive Manufacturing
LPBF	Laser Powder Bed Fusion
P	Laser Power
v	Scan Speed
t	Layer Thickness
h	Hatch distance
ANSI	American National Standard Institute
AMSC	Additive Manufacturing Standardization
ASTM	American Society for Testing Materials
ISO	International Organization for Standardization
DED	Direct Energy Deposition
$\boldsymbol{\varepsilon}$	Cooling Rate
R	Solidification Rate
G	Temperature Gradient
LOF	Lack of Fusion
M_w	Melt Pool Width
M_d	Melt Pool Depth
T_f, T_m	Melting Temperature of the Alloy
T_0	Temperature far from melt pool
T_b	Boiling Temperature of the Alloy
Q	Absorbed Power
k	Thermal Conductivity
α, D	Thermal Diffusivity
r	Distance to Edge of Melt Pool
ξ	Distance from Heat Source
$\Delta H/h_s$	Normalized Enthalpy
η, A	Absorptivity
ρ	Density
C_p	Specific Heat Capacity
L	Latent Heat of Fusion
h_s	Enthalpy at Melting
σ	Laser Beam Size
SSGBs	Solidification Subgrain Boundaries
SGBs	Solidification Gran Boundaries
MGBs	Migrated Grain Boundaries
k	Equilibrium Distribution Coefficient
C_s	Solid Composition
C_l	Liquid Composition
SLM	Selective Laser Melting

d_{xx}	Average Particle Size Distribution at xx%
C_{pM}	Effective C_p of Melting
C_{pL}	Effective C_p of Vaporization
t_{max}	Intersecting point between adjacent melt pools
SEM	Secondary Electron Microscopy
BSE	Backscatter Electron Microscopy
WDS	Wavelength Dispersive Spectroscopy
MSDS	Materials Safety Data Sheet
LED	Linear Energy Density
VED	Volumetric Energy Density
EDM	Electrical Discharge Machine
UTS	Ultimate Tensile Strength
YS	Yield Strength

TABLE OF CONTENTS

Page

LIST OF FIGURES

Page

LIST OF TABLES

Page

CHAPTER I
INTRODUCTION

1.1 Background

1.1.1 Current State of the Manufacturing Industry

U.S. manufacturing is one of the most important sectors of the U.S. economy and is a measure of a nation's economic health in terms of total gross output and employment. In 2017, the manufacturing industry nominal value added[1] was $2.245 trillion (11.4% of the total U.S. gross domestic product) [1]. By the second quarter of 2018, the manufacturing industry generated $2.33 trillion in nominal value added, which was a 7.5% increase from the second quarter of 2017 [1]. As of September 2018, there were 12.8 million workers directly employed in manufacturing accounting for 12 percent of the total U.S. workforce [2]. Furthermore, the Bureau of Economic Analysis reported that manufacturers in the U.S. perform more than three-quarters of all private-sector research and development in the U.S. making it one of the most innovative sectors. As the next era of the industrial revolution takes place, also known as Industry 4.0, it is estimated that nearly 3.5 million manufacturing jobs will be needed by the year 2025. Of those 3.5 million jobs, about 2 million of those jobs will go unfilled [3]. Furthermore, executives claim that about 67% of their current employees do not have sufficient, fundamental technical skills in the manufacturing field [3].

One major advanced manufacturing technique that has emerged in Industry 4.0 is additive manufacturing (colloquially known as 3D printing). The field of metal additive manufacturing (AM) has grown substantially over the past several decades and has created valuable opportunities

[1] According to the Bureau of Economic Analysis, nominal value added is the difference between the gross output of an industry and its intermediate inputs. Nominal value added is the contribution of an industry to GDP [1].

primarily in the automotive, aerospace and defense, and medical device industries [4]. These industries typically exhibit low production volumes, highly customized parts, and in some cases a high number of components. These characteristics make AM a suitable alternative over traditional manufacturing where there is opportunity to eliminate multiple assembly steps, reduce material waste, reduce the number of components, and improve lead time for functional, end-use parts. However, metal AM is limited by the selection of materials that can be successfully printed due to the differences in thermophysical properties of various alloys and their response to nonuniform heating and cooling under commonly used process condition [5, 6].

Recent research and development efforts have focused on designing new materials for AM to meet industry applications. As alloy development for AM continues to evolve, there is a need to make efficient and strategic decisions to optimize operating parameters for new materials and understand the process, structure, and property relationships of new materials. The contribution of this work is to develop and validate a process-specific guideline for printing new alloys using a specific metal AM process known as laser powder bed fusion (LPBF). This process will be discussed in further detail in **Section 1.2**.

1.1.2 Additive Manufacturing in Industry 4.0

The Fourth Industrial Revolution, also known as Industry 4.0, involves the integration of advanced technologies that are physically and digitally connected. This means that manufacturing is transitioning from manual tasks to automated tasks where machines will be able to communicate with one another, information will be collected and analyzed, and that information will be communicated back to the machine to optimize the process and make it more efficient.

Not only will machines be connected to one another, but entire facilities and organizations as well as their customers and partners will be integrated into a digital supply network [7, 8].

Digital supply networks will generate opportunity and growth for businesses by improving productivity and adapting to dynamic changes in supply and demand. Industry 4.0 allows organizations to maximize their asset utilization as well as reduce risk associated with recalls, part failures, and managing excess inventory. Companies that integrate new technologies that fit within Industry 4.0 will have the competitive advantage in identifying new opportunities and creating new products to meet customer expectations.

As mentioned above, AM is an evolving technology within Industry 4.0. There are four major target areas of AM as outline by the America Makes Technology Roadmap, version 2: 1. Design, 2. Material, 3. Process, and 4. Value Chain [9]. Each target area focuses on unique challenges. For instance, designing parts for AM requires knowledge of the advantages and disadvantages of conventional manufacturing versus AM processes. In other words, is a certain part more suitable for traditional manufacturing or AM? Additionally, design engineers also need to consider part orientation, support structures, overhangs, etc., to minimize post-processing tasks. As new materials are being developed for AM, there is a need for creating a database that collects material properties and their respective mechanical properties. Furthermore, there is a need to develop accurate models to aid in selecting the appropriate process parameters for new materials as well as to better predict part failure and defects during the printing operation. The process target area focuses on improving detail, resolution (or surface finish), and porosity defects. As AM becomes more industrialized, there is also a need for building machines that can print with larger build

volumes. The value chain segment focuses on the cradle-to-grave approach of the entire AM process. The value-chain is concerned with making improvements to reduce costs and improve time-to-market capabilities. From the four target areas summarized above, this work contributes to the Materials and Process target areas.

1.1.3 Additive Manufacturing – Current State of the Industry

According to the 2018 annual report published by Wohlers Associates, the report shows an average annual growth of 26.6% of the overall AM market since 1989. The annual growth in 2017 for all AM products and services was 21.0% ($7.336 billion). Furthermore, industrial systems selling for more than $5,000 grew by 12.6% (14,736 unit sales) as compared to 4.0% in 2016 (13,084 units sales). More specifically, metal AM systems markets grew by 79.9% from 2016 to 2017. Sales for metal materials grew 44.6% ($183 million) out of the total AM material sales which increased 25.5% ($1.13 billion). The Wohlers Report summarized that companies spent approximately $918.6 million on AM for end-use parts in 2017, making AM for final part production grow 32.4% in 2017 [4] .

Currently, there are two major categories of materials used for AM: polymers and metals. This thesis will focus on metal AM. **Table 1** lists current metal materials used for AM [4]:

Table 1. Materials used in AM

Metal Materials for AM
Steels
Stainless Steels
Titanium Alloys
Aluminum Alloys

Table 1, Continued. Materials used in AM

Metal Materials for AM
Nickel-based Alloys
Cobalt-Chromium Alloys
Copper-based Alloys
Gold
Silver
Platinum
Palladium
Tantalum

Trends in material development show a higher focus on copper and aluminum alloys while steels, titanium alloys, and nickel-based alloys are still being highly investigated. Debroy *et al.*, provide a strong overview of research on various metal alloys for AM in their review article [10]. This work focus on a binary nickel alloy ($NiNb_5$). Part of this work was funded by the Air Force Research Laboratory and thus, nickel alloys are widely used in the aerospace industry due to their high strengths at high temperatures and excellent corrosion resistant properties.

1.1.3.1 Additive Manufacturing Standards

America Makes is an organization that brings together members from industry, academia, government, and workforce to accelerate AM technology in the U.S. America Makes and the American National Standards Institute (ANSI) joined together to create the Additive Manufacturing Standardization Collaborative (AMSC). Every year, AMSC publishes a road map to assess the state of AM industry in the four target areas mentioned above. The roadmap highlights key industry gaps and research needs in order to pave the way for industrial adoption of AM.

The American Society for Testing Materials (ASTM International) and the International organization for Standardization (ISO) are also organizations currently developing standards for AM. Although some standards have not been officially published, the following organizations and standards listed in **Table 2** are relevant to AM and should be studied upon release [11]:

Table 2. List of standards relating to AM

Standards		
Standard	**Title**	**Status**
ISO/ASTM 52900:2015	Additive manufacturing – General principles - terminology	Published
ISO/ASTM 52921:2013	Standard terminology for additive manufacturing – Coordinate systems and test methodologies	Published
ISO/ASTM DIS 529211-1 (ASTM F42)	*Additive manufacturing – Technical design guideline for powder bed fusion – Part 1: Laser-based powder bed fusion of metals*	*Under Development*
AMSC Roadmap, version 2	Standardization road map for additive manufacturing, version 2.0	Published

Although several research studies have contributed to developing a process parameter guideline, there has not been a formal standard published for LPBF users. This work contributes to the

current research on creating a framework for LPBF users to print new materials while minimizing computational and experimental trial and error.

1.2 Metal Additive Manufacturing Process Overview

AM is a manufacturing process that builds a part layer by layer as opposed to subtractive manufacturing or conventional manufacturing methods. The advantage of AM is the ability to produce parts with complex geometries that cannot be produced by any other means (i.e., lattices, meshes, intricate internal pathways such as those in heat exchangers, etc.). AM is capable of building all-in-one assemblies; in other words, a typically assembly may have well over twenty individual components if it were manufactured using conventional methods. By employing AM technologies, the same assembly can be fabricated as a single component which ultimately reduces points of failure, labor time, and costs. Since complex geometries such as lattices can be created, many components can be drastically reduced in weight. Reduction in lead-time is another major advantage of AM.

Although AM shows strong advantages, there are currently many challenges researchers and industry operators face. For instance, parts are difficult to qualify due to machine-to-machine variability as well as batch-to-batch variability. Porosity is also a major challenge that is often seen in final AM parts. Thus, post-processing is often required, which increases the lead time and cost of the part due to additional processing and labor. Additional finishing steps such as removing the part from the substrate, removing the supports, polishing, grinding, and machining may also be required. AM machines are also limited in build size and therefore, AM is more suitable for low production volumes and smaller components. Besides process challenges, computational

models prove to be helpful in optimizing the process but are often time consuming and expensive as the accuracy and complexity of the model increases. Simplified models, such as the Eagar-Tsai model, have been used to decrease computational time to aid in the process parameter selection process.

Two of the major metal AM techniques that have been employed are direct energy deposition (DED) and LPBF. The major difference between the two processes is the way the powder is deposited. In DED, the powder is directly deposited through four nozzles onto the object and simultaneously melted with a laser to create a single layer of the printed part. The laser-head system incrementally moves up in the z-direction to print each layer. A key advantage of the DED system is that the machines can deposit up to four different materials or combinations of materials at once. Furthermore, the DED system can produce functionally-graded materials in which one part of the material is composed of a certain metal and gradually changes to a different metal on the other half of the part. In comparison, the LPBF process has a roller and scraper that spreads a layer powder of desired thickness across a bed and then the laser selectively melts regions of the powder bed to create a layer of the object. The object lowers into the chamber and the process repeats itself until the final part is created. A labeled image of the inside of the LPBF system used for tis research is shown in **Figure 1**. The advantages of LPBF is the higher resolution, surface finish, and complex details that can be achieved. LPBF is also more commonly used in industry to manufacture end-use parts.

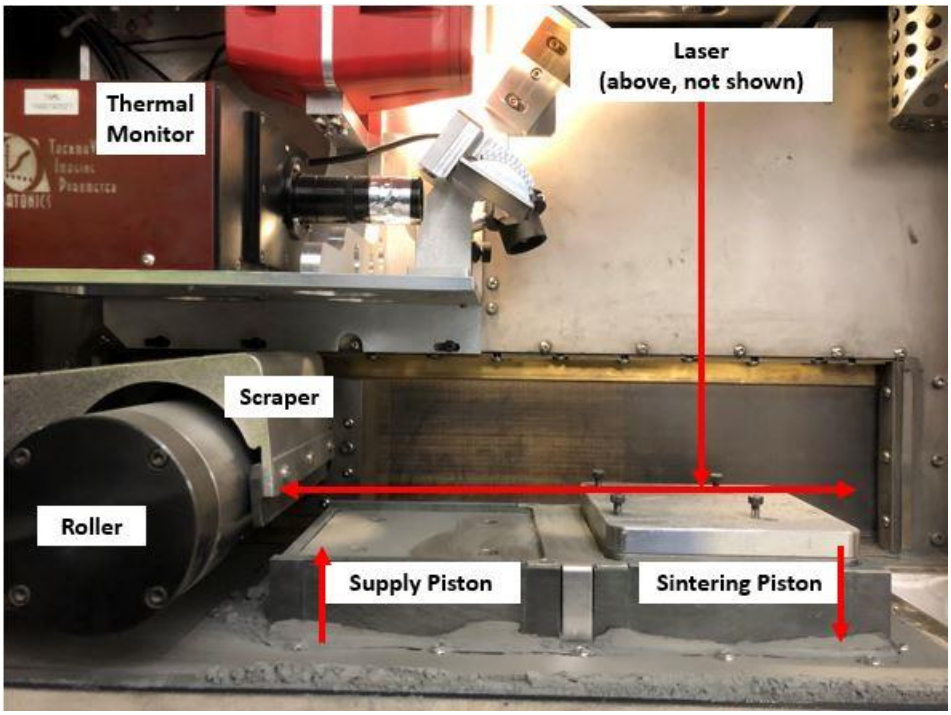

Figure 1. A photo of the inside of the LPBF system.

1.3 Problem Statement and Objective

The objective of this thesis is to provide a guideline for LPBF operators that aids in the process parameters selection process for new materials. At the end the thesis, a link to a completed spreadsheet as well as a template spreadsheet for a new material will be provided. The spreadsheet provides a detailed approach of the information that needs to be collected, how the information can be used to plan experiments, and how to analyze the data. The spreadsheet also includes links to images and data collected during the characterization processes of each specimen.

The motivation to develop a guideline for printing new materials is to address the following problem statement:

How can laser-powder bed fusion process parameters be determined for new materials such that low porosity parts are fabricated while minimizing computational and experimental trial and error?

1.4 Organization and Structure of Thesis

This thesis is broken down into six chapters. Chapter 1 provided a brief overview of AM and how it fits within the scope of Industry 4.0. The first chapter also discussed the current state of the AM industry and its projected growth in the next several years. Finally, the chapter ended with the problem state that the remainder of this thesis addresses.

Chapter 2 provides an overview of previous research that has contributed to the developing a framework for printing new alloys for AM. The chapter also includes an overview of the process, microstructure, property relationship - which is seen as a recurring theme in this thesis.

Chapter 3 reveals the guideline and walks the reader step-by-step through the process. The framework builds upon previous studies that have studied the relationship between process parameters and materials with various thermal physical properties. This section serves as a template guideline for new materials. Each step of the guideline is discussed in detail but the section does not provide parameter values and material properties as these are dependent on the material. Determination of the process parameter values and material properties are discuss in detail in Chapter 4 where $NiNb_5$ is the material under investigation in this study. Chapter 4 uses the steps outlines in Chapter 3. A detailed write-up of the design of experiments as well as the characterization methods of the raw powder, single tracks, and builds are discussed. In Chapter

4. **Appendix A** will provide the reader with an excel spreadsheet that contains data collected for $NiNb_5$ as well as a template spreadsheet for new materials.

Chapter 5 provides a critical analysis of the data collected from experimental work in chapter 4.

Chapter 6 concludes the thesis by summarizing key outcomes and by providing suggestions for future work in this research area.

CHAPTER II
LITERATURE REVIEW

2.1 Relationship Between Process, Microstructure, and Properties in LPBF

When new materials are printed, it is important to gain an understanding of how the LPBF process dictates the microstructure and how the microstructure affects the property of the build. Various parameters of the same material may lead to a variety of microstructural and physical property outcomes. Microstructural features are dependent on the solidification conditions and physical phenomena occurring within the melt pool [12]. Here, we primarily focus on the heat transfer, solidification, and physical phenomena occurring during the LPBF process. We then briefly discuss how the thermophysical conditions govern the microstructure and physical properties of a build. Several reports and review articles on metal AM process, microstructure, and properties have been published as serve as great starting points for new AM users or great refreshers for experienced AM operators [1-15]. This thesis investigates the process, structure, and property relationship of $NiNb_5$; therefore, this section will focus on nickel-based alloys. Nickel alloys are known for their high strength and corrosion-resistance properties at elevated temperatures.

2.1.1 Heat Transfer, Solidification, and Fluid Flow Phenomena

As the laser scans the powder bed surface, the phase transition from solid powder into a molten liquid melt pool is induced [12]. As the laser continues along its path, the trailing melt pool solidifies. There are three fundamental solidification parameters to consider as described in **equation 2.1**

$$\varepsilon = GR \qquad \textbf{2.1}$$

where ε is the cooling rate, R is the solidification rate, and G is the temperature gradient [26]. These solidification conditions are controlled by the process parameters (P, v, t, and h) and greatly influenced by the inherent thermophysical properties of the alloy. The laser power and speed determine the shape and size of the melt pool geometry which affects the thermal gradient in successive layers as well as the resulting grain size [27]. Furthermore, the modes of heat transfer change throughout the build process. Mukherjee *et al.* explained that the first layer of the build experiences a high rate of heat transfer between the molten pool and the solid substrate because the solid substrate has higher conductivity than that of the powder [3 - 4]. The powder surrounding the melted regions acts as thermal insulator and therefore, as the laser makes adjacent passes within the same layer, high heat transfer occurs through the already deposited, solidified regions and the substrate. Conversely, low heat transfer occurs between the molten pool and the powder [28]. The maximum heat transfer occurs as more layers are joined where heat accumulates through the already solidified region below the molten pool toward the substrate [3 - 4]. A summary of heat transfer through different phases of the build process is illustrated in **Figure 2**.

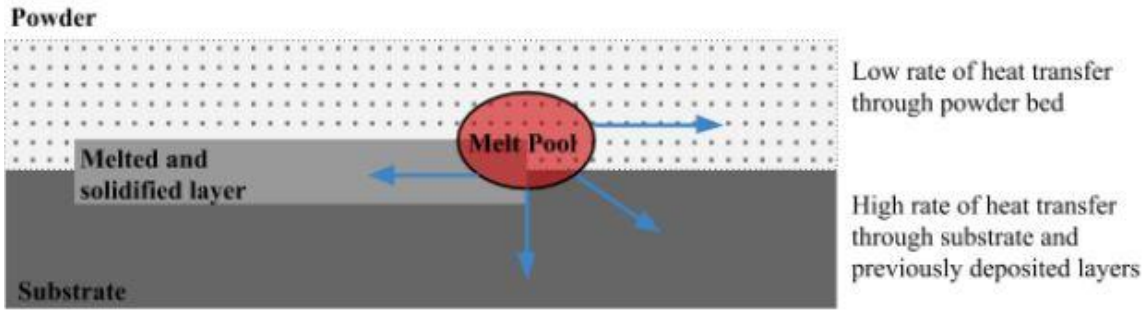

Figure 2. Figure showing rate of heat transfer through the powder bed, the substrate, and the solidified structure.

Heat transfer between the molten pool and the solid regions is governed by conduction and is typically accounted for in most thermodynamic models for AM. More complex models include convective heat transfer (i.e., the heat transfer within the melt pool and its surroundings) which is governed by capillary forces and surface tension fluid flow. The surface tension fluid flow is also referred to as Marangoni flow [5 – 8]. The direction of fluid flow determines the geometry and depth of the melt pool. For wide and shallow melt pool depths, the fluid flow pattern can be described as an outward motion from the center to the surface edges of the pool. In other words, surface tension will be lowest in the center of the melt pool (i.e., where heat transfer is the greatest) and will be highest on the coolest part of the surface of the melt pool (i.e. where heat transfer will be lowest) [9 - 10]. This is because surface tension decreases as temperature increases. This type of Marangoni flow is seen for pure metals and most alloys. The result of a melt pool that is too shallow will lead to lack of fusion (LOF). Lack of fusion occurs when there is insufficient overlap in successive melt pools [34]. In order to mitigate LOF, previous studies reported two main criteria: 1) the melt pool depth needs to be at least as large as the layer thickness, and 2) the hatch distance cannot be too large [34]. These criteria are summarized in **Equation 2.2**

$$(H/W)^2 + (L/D)^2 \leq 1 \qquad \textbf{2.2}$$

where H is the hatch spacing, W is the melt pool width, L is the layer thickness, and D is the total melt pool depth [35]. The melt pool dimensions in the study by Tang *et al.* were estimated using the analytical Rosenthal equation [36]. The study also reported that material properties at room temperature were better aligned with the experimental melt pool dimensions [34].

$$T_f = T_0 + \frac{Q}{2\pi kr}\exp[-\frac{V(\xi+r)}{2\alpha}]$$ Rosenthal's Equation **2.3**

where T_f is the melting point of the alloy, T_0 is the temperature far from the melt pool, Q is the absorbed power, k is the thermal conductivity, V is the beam speed, and α is the thermal diffusivity. The shape and size of the melt pool are defined by r and ξ, where $r = (\xi^2 + y^2)^{0.5}$ is the distance to the edge of the melt pool and ξ is the distance from the heat source [32, 34].

Some alloys contain elements that become surface active in the molten pool. These elements will segregate to the surface and lower the magnitude of surface tension (i.e., surface tension will increase with increasing temperature) [33]. The result is an opposite Marangoni flow pattern described above. Heat transfer will circulate inward from the outer edges of the melt pool to the center, yielding a deep, narrow melt pool [33].

A third type of melt pool geometry can be described and is referred to keyhole mode, or keyholing. Keyholing is an undesirable melt pool feature that occurs when the heat input is very large for a small area in the powder bed. This high energy density produces very deep and narrow melt pool depths [33]. Keyholing can be identified in the final part because it often contributes to porosity issues. For high energy densities, the peak temperature of the melt pool will increase to boiling point of the material. At the same time, the vapor pressure will rise exponentially with temperature. When the temperature approach the boiling point of the metal, a cavity near the tip of the melt pool will form due to the liquid moving away from the heat source (i.e., due to the recoil momentum pressure due to vaporization) [37]. The result leaves a porosity defect in the final build that is approximately cylindrical and resembles the size and shape of the beam [33].

Studies from Wanye *et al.* and Hann *et al.* present criteria for determining the threshold for keyhole mode [27, 28]. The criteria presented below was what we adapted for part of the process parameter guideline in Chapter 3. **Equation 2.4** simply says that if the melt pool depth is equal or larger than half the melt pool width, we can predict that onset keyholing will occur [37]. Additionally, it was found that when normalized enthalpy ($\Delta H/h_s$) was greater than 30, we would also begin to observe onset keyhole mode [27, 28].

$$M_d \geq \frac{M_w}{2} \quad or \quad \frac{2M_d}{M_w} \geq 1 \qquad \textbf{2.4}$$

$$\frac{\Delta H}{h_s} \geq 30, where \ \frac{\Delta H}{h_s} = \frac{AP}{\rho h_s \sqrt{\pi D v (\frac{\sigma}{4})^3}} \qquad \textbf{2.5}$$

Table 3. Material properties, symbols, and units

Property	Symbols	Units
Absorptivity	A	0 - 1
Density	ρ	(kg/m^3)
Thermal Diffusivity	D	(m^2/s)
Specific Heat Capacity	C_p	(J/(kg*K))
Latent Heat of Fusion	L	(J/kg)
Enthalpy at Melting	h_s	(J/kg)
Laser Power	P	(W)
Scanning Speed	v	(m/s)
Laser Beam Size	σ	(μm)
Melt Pool Depth	M_d	(μm)
Melt Pool Width	M_w	(μm)

From the discussion above, we can realize that analytical and numerical models for predicting melt pool features is incredibly important. We also need to understand how changes in process

parameters, specifically P and v, influence Marangoni fluid flow and ergo, yield sufficient melt pool depths. Melt pools that are too wide and shallow will lead to lack of fusion to the previous layer and depths that are too large and narrow will also lead to lack of fusion and porosity issues. Metal AM has strongly relied on previous welding literature and many researchers have developed analytical and numerical models for understanding heat flow [11 - 30]. Tsai reported an analytical solution for a heat source with Gaussian distribution on a finite plate [22, 25]. Later, Eagar and Tsai developed an analytical solution for determining the temperature fields for travelling heat source [58]. This model would later lay the foundation for current research in metal AM. The Eagar-Tsai model was used for the research presented in this thesis.

The Eagar-Tsai model is a simplified heat transfer model that was originally used in the welding community and has shown to be promising for predicting the melt pool geometries during LPBF techniques. The model assumes a Gaussian beam on a flat surface but only takes non-temperature dependent material property values. The model does not consider convective heat transfer and thus, cannot predict keyholing. The advantage to using the Eagar-Tsai model is that it is inexpensive and can run 100s of trials in a short amount of time [56].

2.1.2 Microstructural Evolution in Nickel Based Alloys

The microstructure of alloys fabricated via AM processes is much more complex than microstructures from conventional welding and casting due to the rapid solidification and multiple reheating and remelting cycles. However, we can rely on concepts from welding metallurgy to gain a better understand of what is occurring in AM builds. This section provides an overview of the microstructure of nickel based alloys. This section provides a good foundation

for what we may observe in binary nickel alloys (e.g., NiNb, NiAl, NiCu, and NiZr). An in-depth discussion of the microstructure of various nickel alloys can be found in *Welding Metallurgy and Weldability of Nickel-base Alloys* [12].

The face-centered cubic structure of nickel (γ) can be precipatation strengthened when alloyed with elements such as: NiAlTi, NiCuAlTi, NiCrAlTi, NiCrNb, and NiFeCrNbAlTi [12]. Summarized from the welding literature, some nickel alloys will show microstructures consisting of γ dendrites with γ' precipitates and γ/γ' at the SSGB. The γ/γ' eutectic typically leads to low surface energy and strain energy which in turn results in low activation energy. When the activation energy is low, the rate of nucleation increases and thus, we see γ' formation. The size and density of the precipitates are determined by the rate of cooling from the processing parameters. As the rate of the cooling increases, the size of the precipitates become smaller [12].

Nickel alloys can be solid solution hardened when combined with the following elements: NiNb, NiCu, NiMo, NiFe, NiCrFe, NiCrMoW, NiFeCrMo, or NiCrCoMo [12]. As these alloying elements segregate during solidification, the resulting microstructure will contain localized compositional changes at the subgrain level which may induce several types of grain boundaries conditions [59]. One type of boundary condition that may be observed is solidification subgrain boundaries (SSGBs) which are identified as cells or dendrites. These features typically have a different composition than the bulk material [1, 47]. Competitive grain growth results in solidification grain boundaries (SGBs, not to be confused with SSGBs) that occur along the trailing edge of the melt pool. SGBs are different than SSGBs because they have greater misorientation along the grain boundaries which give rise to dislocation networks along the grain

boundary [1, 47]. A third interface that may exist is migrated grain boundaries (MGBs). MGB have even greater misorientation along the grain boundaries than SGBs and are often seen in fully austenitic welds [1, 47].

Dendritic structures and intermetallic compounds that form in nickel alloys are of particular interest [10, 60–65]. The phases that form along the dendritic boundaries and within the interdendritic regions occur during solidification and are dependent on alloy composition, process parameters, and the temperature gradient [12]. Several studies have reported that the equilibrium distribution coefficient (k) is an important value for quantifying how much an alloying element will partition into the liquid and solid phases during solidification [12].

$$k = C_s/C_l \qquad \textbf{2.6}$$

where C_s is the solid composition and C_l is the liquid composition at a specific temperature. Alloying elements tend to segregate to the liquid phase when $k < 1$.

The size and morphology of grain boundaries have a significant effect on the mechanical performance of a material. For instance, fine grains may or may not be desirable depending of the operating conditions. If the fine grain material is exposed to high temperatures and low strain rates, deformation along the grain boundary can occur. However, if the same fine grain material is exposed to low temperatures and high strain rates, the grain boundaries will become hardened and as a result, increase the strength of the material [66].

2.1.3 Mechanical Testing of SLM Fabricated Nickel Alloys

Many studies have been done on SLM of Inconel 625 and Inconel 718. The material under investigation in this thesis is $NiNb_5$ and closer to pure nickel (or nickel 200) than Inconel. A limited number of studies have been able to print pure nickel specimen with 98 percent density or greater [35, 36]. Yap *et al.* reported that better density results were obtained with higher laser powers, slower scan speeds, and smaller hatch spacings [68]. The paper also reports that pure nickel processed via SLM showed a 40 percent increase in ultimate tensile strength and 2 – 3 times greater yield strength than that of pure nickel. However, the ductility of the SLM nickel decreased 10 – 30 percent compared to its pure nickel counterpart [68]. Similar results were shown for Inconel 625 and therefore, should be a good indication of what we should observe for $NiNb_5$ [69]. The reason for the increase in strength and decrease in ductility is most likely attributed to the small crystal grains that inherently provide more grain boundaries. As the number of grain boundaries increase, dislocations are not able to mobilize, resulting in grain boundary strengthening [68]. As we would expect, as porosity decreased, the tensile performance improved.

CHAPTER III
PROCESS PARAMETER SELECTION GUIDELINE

This section presents the process parameter selection guideline for new materials (**Figure 3**). This guideline is incredibly useful for new graduate students doing work in AM, specifically with new alloys. One goal of this framework is that it will expedite the process in which successful (near full dense) parts can be created for further testing and analysis. Each step outlines the data that needs to be collected and/or the method that needs to be carried out. The steps are applied to $NiNb_5$ to provide an example of how we obtain certain values.

PROCESS PARAMETER SELECTION GUIDELINE

STEPS & DATA COLLECTION

STEP 1

1. Determine material properties.

Material Property	Symbol	Units
Melting Temperature	T_m	K
Boiling Temperature	T_b	K
Thermal Conductivity	k	W/(m*K)
Specific Heat Capacity	C_p	J/(kg*K)
Absorptivity	η	0 - 1
Density	ρ	kg/m³

STEP 2

2. Determine upper and lower bounds of process paramters.

Process Parameter, Symbol, (Units)	Machine Limitations	Process Parameters Based on Material Properties
Laser Power, P, (W)	0 - 265	65 - 472
Scan Speed, v, (mm/s)	0 - 2500	0.0001 - 2500
Layer Thickness, t, (μm)	20 - X	30 - $1.5d_{max}$
Hatch Distance, h, (μm)	30 - $2M_w$	(50% of M_w) - (t_{max} = 30 μm)

Min and max power and scan speed depend on material properties.

STEP 3

3. Conduct design of experiments (DOE) for single tracks using Eagar-Tsai model.

Latin hypercube sampling (LHS) for the region of interest.
Evenly spaced sampling for outside region of interst.

STEP 4

4. Perform single track experiments with various P and v combinations. Measure melt pool widths and depths and compare to predicted values.

Standard for melt pool measurements	
M_w	Measure width from left to right where melt pool joins the surface of the substrate.
M_d	Measure depth from point normal to the surface of the substrate to the top of the melt pool below the substrate.

STEP 5

5. Calibrate the Eagar-Tsai material properties to match experimental melt pool width.

Calibrate using a surrogate model.
Calibrate the following material properties: *thermal conductivity, specific heat capacity, and*

STEP 6

6. Determine which parameters are good candidates for printing near full-dense parts.

Look for single tracks with melt pool widths that are consistent (i.e., have little variation) along the length of the track. (Top view .)
Look for melt pool depths that meet the following criteria to avoid keyhole mode: $M_d > M_w/2.5$ or $\frac{\Delta H}{h_s} \geq 30$.

STE P 7

7. Determine set of cubes to print. Optimize hatch distance to reduce build times. while maximzing density.

Minimum hatch spacing is 50% of the melt pool width.
Maximum hatch spacing is the distance that produces a t_{max} value equal to the layer thickness (e.g., 30 μm).

STEP 8

8. Print cubes for microstructural and differiential evaporation analysis.

Print 10 x 10 x 10 mm cubes.
Measure density of cubes using Archimedes method.
Perform microstructural analysis of side and top cross-sections using SEM/BSE.
Measure differential evaportion os element(s) using WDS.

STEP 9

9. Determine mechanical properties of new material.

Print 34 x 10 x 11 m blocks.
Cut tension and compression samples. Perform tension and compression tests to determine yield strength, ultimate tensile strength, and elongation.

Figure 3. Process Parameter Guideline - Step and Data Collection.

3.1 Determine Thermophysical Material Properties

Before the printing process can begin for a new alloy, it is important to know several critical thermophysical material properties. These properties include melting temperature (T_m (K)), thermal conductivity (k (W/(m*K)), specific heat capacity (C_p (K/(kg*K))), and absorptivity (η (0-1)). An additional material property, density (ρ) is also required. The relationship between process parameters and material properties influences the final microstructure of the build as well as the final mechanical behavior the material. For instance, it is required that the laser power completely melts the powder; however, too high of power may lead to evaporation of certain elements which could produce a shift in composition and lead to undesirable phases or intermetallics that are difficult to mitigate [10] . Too high of heat input could also lead to undesirable keyhole effects. Therefore, knowing the melting temperature, as well as the boiling temperature, of the material gives insight in determining the appropriate laser power.

The remaining three thermophysical material properties are important in order to understand differences in melt pool geometry as a result of laser power and scan speed. For example, a material with high thermal conductivity will produce smaller melt pool depths. To compensate for this effect, laser power would need to be increased and/or scan speed would need to be decreased. Conversely, the opposite adjustment would have to be made for materials exhibiting low thermal conductivity. The specific heat capacity shows the same trend as thermal conductivity. As specific heat increases the shallower the melt pool depth becomes. Absorptivity has an opposite affect compared to the former two properties; in other words, as the absorptivity increases, the melt pool depth will increase. Lastly, the density of the material is required as an input for the Eagar-Tsai model.

Table 4. Material properties used for $NiNb_5$

Thermophysical Property	Value	Units	Reference
T_m	1703	K	[70]
T_b	3103	K	[71]
k	70.4	W/(m*K)	[72]
C	636.19	J/(kg*K)	[73]
η	0.51	0 – 1	[74]
D	1.24×10^{-5}		
Additional Material Properties			
ρ	8909	kg/m^3	[70]
d_{80}	80	µm	[70]
Machine Settings			
Laser beam spot size	80	µm	[75]
t	30	µm	

3.2 Define Operating Parameters for LPBF Process

In this parameter selection guideline, there are four primary operating parameters for LPBF process that contribute to part density: laser power, P, (W), scan speed, v, (mm/s), hatch spacing, h, (µm)), and layer thickness, t, (µm). These parameters are coupled into two groups: 1) P and v and 2) h and t. We will consider P and v first in order to perform single track experiments. The latter two parameters will be discussed in *Section 3.7.*

3.2.1 Power and Scan Speed

P and v are critical processing parameters that influence the size and geometry of the melt pool [1, 2]. The dimensions of the melt pool are of critical importance in order to control solidification and cooling rates as well as reduce the number of times previous layers are remelted and reheated. Various combinations of P and v change the length, width, depth, and temperature distribution of

the melt pool. Here, focus is drawn toward the width and depth specifically. As expected, the width and depth of the melt pool increases as v decreases and P increases. Conversely, the melt pool shrinks as v increases with constant P or decreasing P.

Theoretically, the minimum and maximum laser power for the 3D Systems ProX 200 is 0 and 300 Watts, respectively. These are referred to as the machine constraints. After testing the laser power, we found that the actual maximum power output on our machine was 265 W. There are functional (or operational) constraints which are determined by the laser-powder interaction. Laser power is determined based on two considerations: 1) a stationary laser and 2) a moving laser. Let's consider a stationary laser first. The minimum laser power is the power required to completely melt the material (i.e., the melt pool reaching T_m). Using the Eagar-Tsai model, which is described in more detail in *Section 3*.3, the minimum laser power (assuming scan speed is 0.0001 mm/s) required to melt a single layer (30 µm) is 65 W. The minimum power required to melt one and a half times of the layer thickness (45 µm) is 80 W. The maximum laser power would be the power required to completely boil the material. In other words, the entire melt pool would be at or above T_b.

Now let's consider a moving laser. The minimum laser power still requires the material to melt but also depends on scan speed. The minimum laser power and scan speed should melt a minimum of one and a half times the layer thickness (45 µm) to ensure the top layer is joined to the previous layer. The maximum laser power and scan speed should produce a consistent melt pool along the length of the path while avoiding keyhole mode. A consistent melt pool is a melt pool that does not show high variability in width and depth along the length of the path. Since the Eagar-Tsai

model cannot predict keyhole mode, we adapted the following equation from King *et al.* [37] to predict onset keyholing:

$$M_d \geq \frac{M_w}{2} \ or \ \frac{2M_d}{M_w} \geq 1 \quad \textbf{2.4}$$

$$\frac{\Delta H}{h_s} \geq 30, where \ \frac{\Delta H}{h_s} = \frac{AP}{\rho h_s \sqrt{\pi D v (\frac{\sigma}{4})^3}} \quad \textbf{2.5}$$

The Eagar-Tsai model does not output melt pool dimensions that meet the criteria from **Equation 2.4**. Therefore, we adjust the criteria to the follow in order to check with Eagar-Tsai results:

$$M_d \geq \frac{M_w}{2.5} \ or \ M_d \geq \frac{M_w}{2.2} \quad \textbf{3.1}$$

Furthermore, welding literature uses the enthalpy at melting which refers to the total heat required to melt a given volume of a weld [78]:

$$h_s = \int C_p dT + L \quad \textbf{3.2}$$

Where L is the latent heat of fusion. We use the rule of mixing to estimate the latent heat of fusion for $NiNb_5$ based on the values of pure metals [79]:

$$L = 292400 * 0.95 + 315400 * 0.05 = 293550 \, J/kg$$

The sensible heat from room temperature to 1700 K is [73]:

$$Ni = \int C_p dT = 788510 \, J/kg$$

$$Nb = \int C_p dT = 422362 \ \text{J/kg}$$

Using the rule of mixing again to estimate the sensible heat, we can calculate h_s:

$$h_s = 788510 * 0.95 + 422362 * 0.05 = 1.06\, x\, 10^6\, J/kg$$

We can consider three conditions for maximum power. First, if we use the values in **Table 5** for $NiNb_5$, in addition to the following conventions: σ = 80 μm and v = 2500 mm/s, we can calculate that the maximum power to melt a single layer (30 μm) is 490 W. The maximum power to melt one and a half layers (45 μm) is 472 W. In the third condition, if we assume the maximum power to be the power required to get the center surface of the melt pool equal to T_b, the we can calculate the maximum power to be 208 W. Considering that the maximum power output of the machine is 265 W, we are limited in testing the first two conditions.

The same approach is applied to following process parameter, scan speed (v). The theoretical minimum speed for a moving laser source is dependent on machine constraints. Here, the lower bound is 50 mm/s (chosen for practicality) and the upper bound is 2500 mm/s. The functional minimum and maximum scan speed depends on laser power and material properties. The minimum speed is the speed that generates the largest possible melt pool before keyhole-mode occurs. The maximum scan speed for a is the speed that melts a layer and a half of powder. Melt pools that are do not sufficiently melt a layer of powder produce an effect called lack of fusion (LOF). A quick way to determine if LOF will occur is if the ratio of layer thickness to melt depth is greater than 1:

$$\frac{t}{M_d} > 1 \qquad \textbf{3.3}$$

The region of interest we are looking to optimize for the combination of parameters P and v is shown in **Figure 4**.

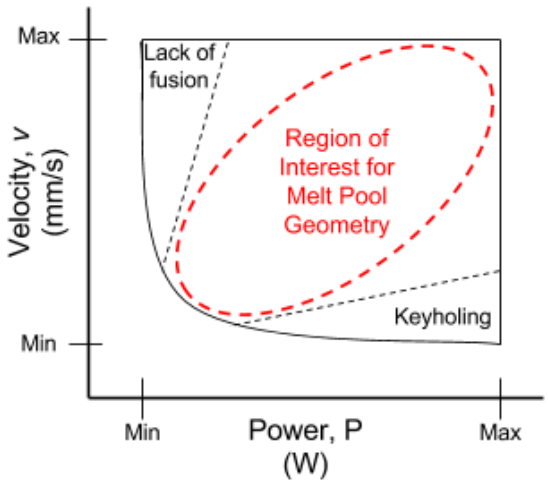

Figure 4. The region of interest is between keyholing (high power and low speed) and LOF (low power and high speed).

3.3 Implement the Eagar-Tsai Model

As mentioned previously, the Eagar-Tsai model was chosen for this guideline because it is computationally inexpensive and many simulations can be run in a relatively short amount of time. One goal is to be able to use this model to define a range of successful P and v parameters and reduce the number of trial and error runs. The model uses a dimensionless form of a travelling Gaussian heat distribution to determine the shape and dimensions of melt pools. The model assumes that the heat source is providing constant energy at a constant speed on an infinite substrate [58]. The limitation of this model is that it excludes the phenomena of convection and cannot predict keyhole mode. Nonetheless, implementing this model can aid in the parameter selection process. The model can predict the melt size (length, width, and depth (μm)) as well as calculate temperature fields of the melt pool. The former output can be used to develop design of experiments to determine a range of process parameters to test with single track experiments. The latter output is useful in eliminating tests from the first output that show how much of the melt

pool reaches boiling temperature. Typically, we will see small amounts of boiling in the melt pool to ensure complete melting of one and a half times the layer thickness. Significant boiling will lead to evaporation of elements and undesirable material properties.

The Eagar-Tsai model requires two sets of inputs: 1) material properties, and 2) process parameters. The model requires the four thermophysical properties mentioned in section 2.1 (T_m, k, c, η) as well as the bulk density of the powder, ρ, (kg/m^3). The model also requires three input process parameters including P, v, and the size of the laser beam at four standard deviations (4σ). We can extract two valuable sets of information from the outputs. First, the melt pool dimensions (length, width, and depth) and second, the temperature field of the melt pool like the example shown in **Figure 5**.

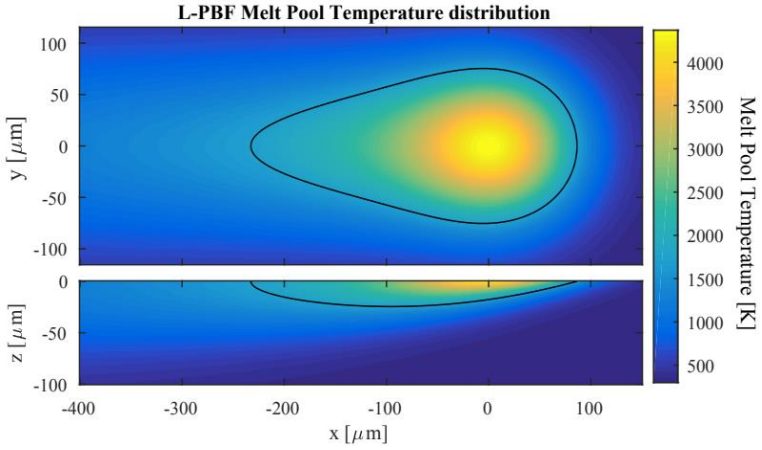

Figure 5. Example of an Eagar-Tsai output showing the temperature distribution of a melt pool for given process parameters.

3.3.1 Design of Experiments for Single Tracks

When the information above (*Sections 3.1 – 3.3*) has been collected, it is useful to begin making a process map with boundary conditions as shown in **Figure 6**.

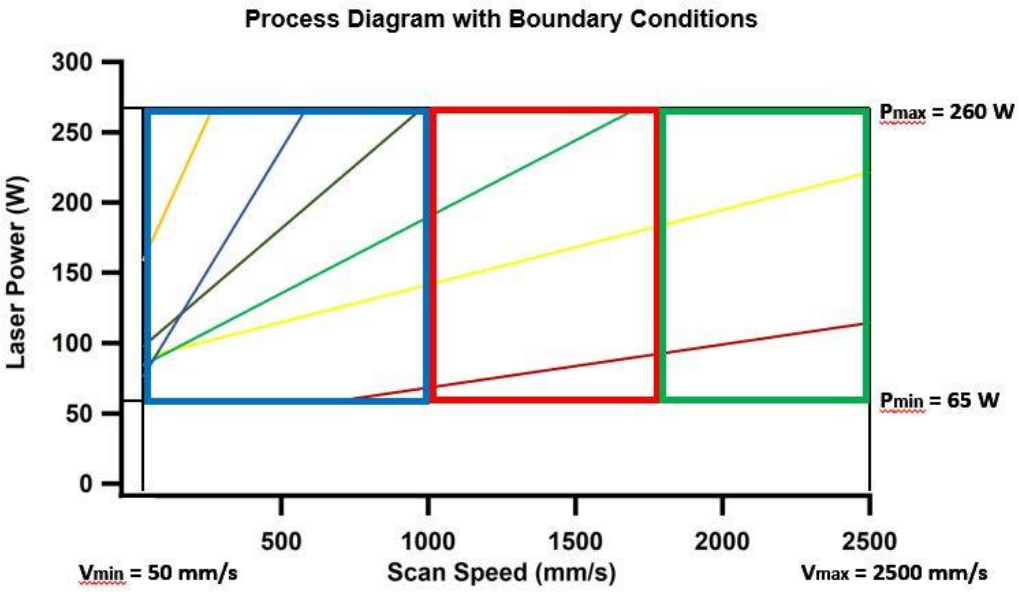

Figure 6. Process diagram with boundary conditions for NiNb single tracks

Table 5. Key for Figure 6 (from top-left to bottom-right)

Color Key	Boundary Condition
Orange	Onset keyhole mode when $M_d = M_w/2.5$ (**Eqn 3.1**)
Dark Blue	Keyhole mode estimated by $\frac{\Delta H}{h_s} \geq 30$
Dark Green	LOF when $M_d = 1.5*t$
Light Green	LOF when $M_d = t$
Yellow	$T_{max} = T_b$
Dark Red	$T_{min} = T_m$

Based off the process map in **Figure 6**, we can see that the optimal range is limited by scan speed (< 1000 mm/s). This is because the dark green boundary line describes the minimum P and v combination before LOF occurs (assuming LOF is less than one and a half times the layer thickness). The optimal region is highlight by the blue box and it is the region we want to test single track experiments in order to validate melt pool dimensions. However, we also want to test outside the optimal region to determine if the parameters would in fact fail (i.e., produce balling or other defects) according to the boundary conditions.

For the optimal region within the blue box, we conducted a Latin Hypercube Sampling (LHS) statistical method to produce twenty random points. The reason we performed LHS is because the method produces evenly spaced points, covers a broad sampling space, and does not generate repeat values. For the red and green non-optimal regions, we chose twelve and eight evenly spaced points, respectively. A summary of points for the optimal and non-optimal regions to be tested are shown in **Figure 7**. The list of parameters can be found in *Chapter 4: Experimental Methods*.

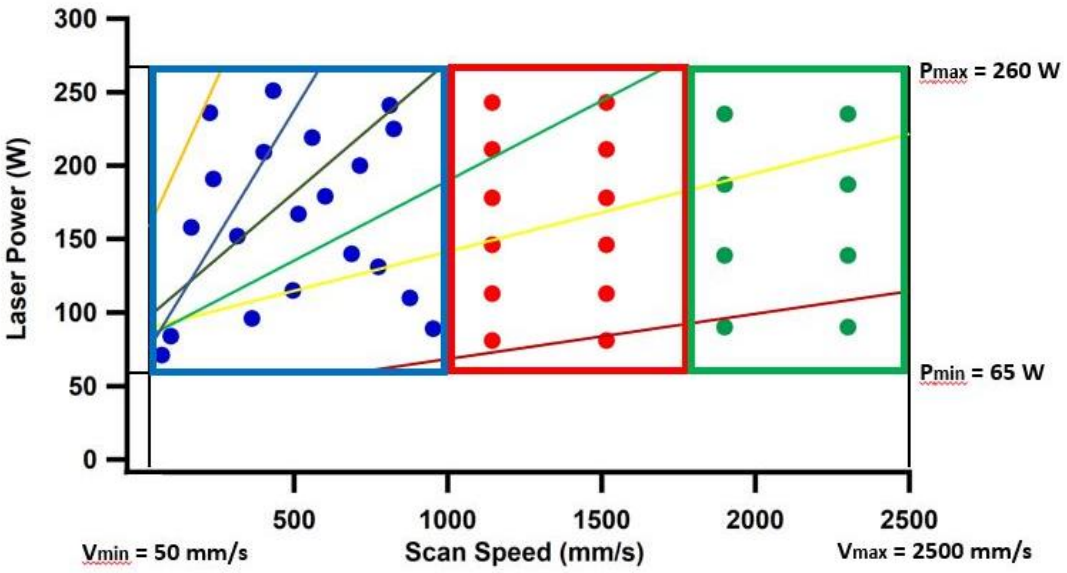

Figure 7. Process diagram with boundary conditions and single track data points.

3.4 Perform Single Track Experiments

Th next step is to run the single track experiments with various P and v parameters that we have chosen in *step 4*. We first additively manufactured a $NiNb_5$ "substrate" on a pure nickel substrate. Once the $NiNb_5$ was built, we printed our single tracks normal to the direction of the substrate scan strategy.[2] The tracks are then cut into three cross-sections and measured for width and depth.[3] The measured melt pool dimensions are then compared to the predicted values produced from the Eagar-Tsai Model.

3.5 Calibrate the Eagar-Tsai Model Inputs

Typically we see melt pool widths that are over-predicted. This is because the model does not consider a layer of powder or convective heat transfer. Therefore, it is necessary to calibrate the

[2] More details on the parameters and dimensions of the $NiNb_5$ can be found in *Chapter 4: Experimental Methods*.
[3] Standards for measuring the width and depth of the singe tracks is also found in *Chapter 4: Experimental Methods*.

model to improve accuracy to the measured results. In order to calibrate the Eagar-Tsai model using the single track measurements, upper and lower bounds were selected for three of the material properties we original listed in **Table 5** (k, C_p, and η).[4] Thermal conductivity values for $NiNb_5$ are bound between the value of the solid and the liquid metal at melting temperature (70.4 W/(m*K), 60.3 W/(m*K)) [79]. Since absorptivity measurements are typically dependent on many factors, including powder size distribution, layer thickness, laser beam profile, and powder material, the actual absorptivity is uncertain [74]. For the purposes of calibration for $NiNb_5$, absorptivity has not been bound and is taken between 0 and 1. The enthalpy of $NiNb_5$ is bound between the effective C_p of melting (C_{pM}) and the effective C_p of vaporization (C_{pL}) of pure nickel (**Figure** 8) and pure niobium (**Figure 9**). The effective C_p of melting is calculated as the slope of the line between the sensible heat at room temperature and the heat required to melt the material. Likewise, the effective C_p of vaporization is calculated as the slope of the line between the sensible heat at room temperature and the heat required to vaporize the material. These lines for nickel and niobium are plotted in the figures below. The effective C_p's are taken as the minimum and maximum of these values for $NiNb_5$ and summarized in **Table 7**.

[4] T_m and ρ are not calibrated since they are taken from the Materials Safety Data Sheet from the supplier.

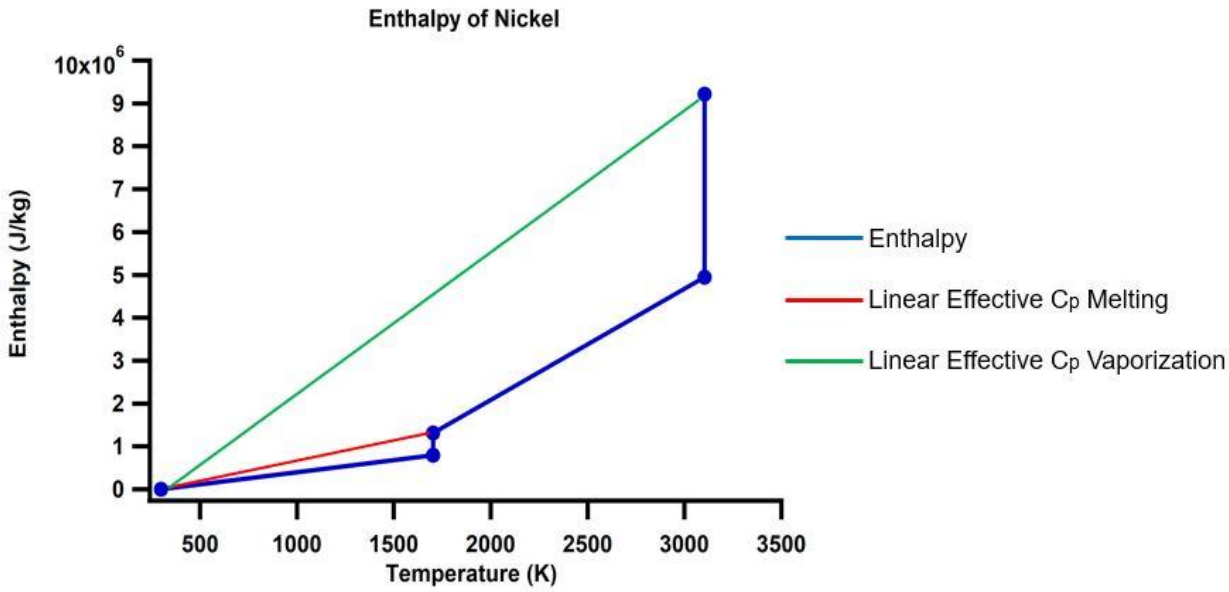

Figure 8. Plot shows the enthalpy of nickel, the linear effective heat capacity of melting, and the effective heat capacity of vaporization.

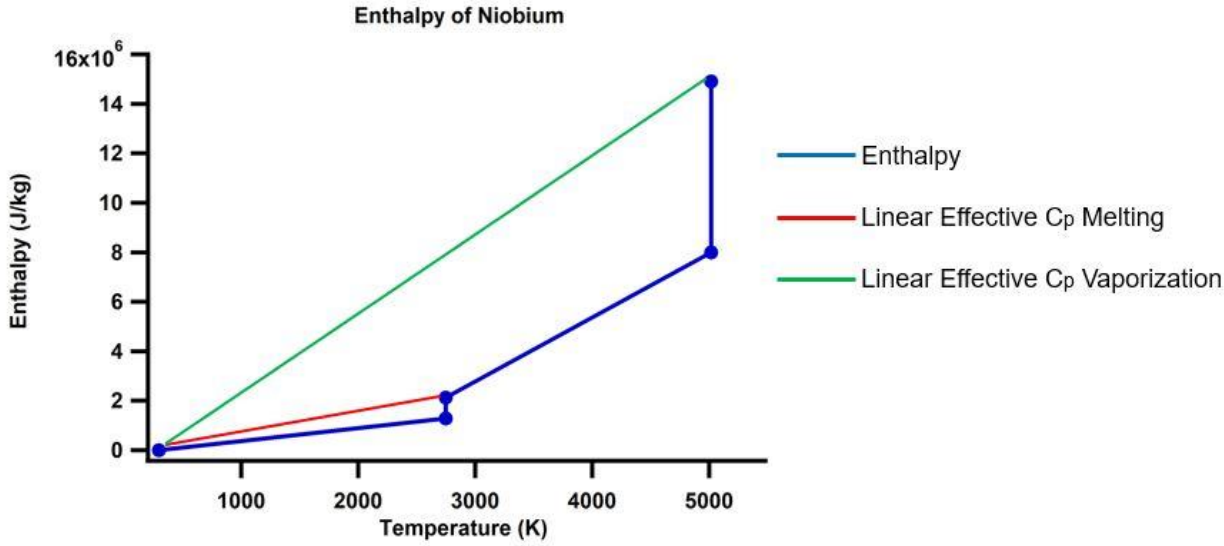

Figure 9. Plot shows the enthalpy of niobium, the linear effective heat capacity of melting, and the effective heat capacity of vaporization.

Table 6. Effective heat capacities of melting and of vaporization

Min and Max Effective C_p	Value	Additional Information	
Min C_{pM}	467 J/(kg*K)	T_m of Nickel	1728 K
Max C_{pM}	772 J/(kg*K)	Tb of Nickel	3003 K
Min C_{pL}	1592 J/(kg*K)	T_m of Niobium	2750 K
Max C_{pL}	2970 J/(kg*K)	Tb of Niobium	5017 K

3.6 Determine Optimal P and v Parameters

After the Eagar-Tsai model is calibrated to better align with the experimental melt pool values, we can determine which P and v parameters are within the optimal range. The following criteria are useful for predicting parameters for printing near full-dense parts:

- Melt pool depths less than the layer thickness will lead to LOF. Parameters yielding depths equal to the layer thickness should be set as the lower boundary condition.
- Parameters yielding depths at least one and half times the layer thickness are good candidates for printing cubes.
- If the melt pool depth is greater than the width/2.5 (**Eqn 3.1**) then the energy density is approaching onset keyhole mode. These parameters should be eliminated. If the depth is equal to the width/2.5 then the parameters should be set as the upper boundary condition or be discarded entirely

3.7 Hatch Distance and Layer Thickness

Once the melt pool geometry is determined, the next parameters to consider are hatch distance and layer thickness. The layer thickness primarily depends on the particle size distribution as well as the shape and surface finish of the particles. For layer thicknesses greater than the maximum

particle size, all particles sizes will be included during the recoating process. Previous studies have shown that large particles impede the ability to achieve efficient packing and increase the likelihood of porosity. Additionally, large particles have been linked to void and crack formation as well as layer separation due to shrinkage after solidification [13, 14]. A smaller layer thickness allows small particles to be distributed during the recoating process while large particles are excluded. The advantage of the latter is increased packing density and lower porosity; however, the adverse consequence is that smaller particles have the tendency to agglomerate [13, 14]. Furthermore, spherical particles are ideal to achieve homogenous melting and uniform layer thickness whereas elongated particles tend to create small voids in the new layer during the recoating process. This is because elongated particles are not able to pack as efficiently as spherical particles. Depending on the powder processing conditions, some feedstock materials may exhibit smooth surface finishes while others may exhibit rougher surface finishes or even satellite particles. The differences in surface finish also affects how well the material will uniformly pack and melt.

The hatch spacing (the distance between adjacent layers) dictates the maximum layer thickness that can be achieved. The maximum layer thickness is determined by the melt pool depth overlap region. The number of times a material is remelted and reheated should also be taken into consideration. The greater the hatch distance the fewer times the previous layers will be remelted and reheated. The more times a material is remelted, the greater the effect of evaporation. However, the drawback to large hatch spacing is that the maximum layer thickness becomes small. Therefore, it is more suitable to have a fixed layer thickness based on particle size distribution and determine the optimum hatch spacing.

As discussed above, the minimum and maximum layer thickness depends on the PSD. The minimum layer thickness is constrained by the average particle size (d_{50}). However, the maximum layer thickness (t_{max}) becomes a function of hatch distance (h), where t_{max} is the intersecting point between overlapping melt pools as shown in **Figure 11**. Note that t_{max} is always smaller than the melt pool depth (M_d) except when h is equal to half the width of the melt pool, then t_{max} equals the melt pool depth (assuming the melt pool is consistent and semicircular). As an example, **Figure 12** shows a comparison of two overlapping melt pools when h is 50µmand 150 um, respectively. In both figures, the melt pools are of the same dimension (width is 250 µm and depth is 60 µm). The resulting t_{max} for each hatch distance is 58 µmand 48 um, respectively. Therefore, both hatch distances would be sufficient if printing with a fixed layer thickness of 30 µm or lower. Larger layer thicknesses can be achieved up until the t_{max} value if desired. The area below t_{max} (i.e., the area in between the two melt pools) is where LOF would occur if the layer thickness is larger than t_{max}. Both cases assume constant laser power and scan speed. We can see that as h increases, t_{max} decreases and vice versa.

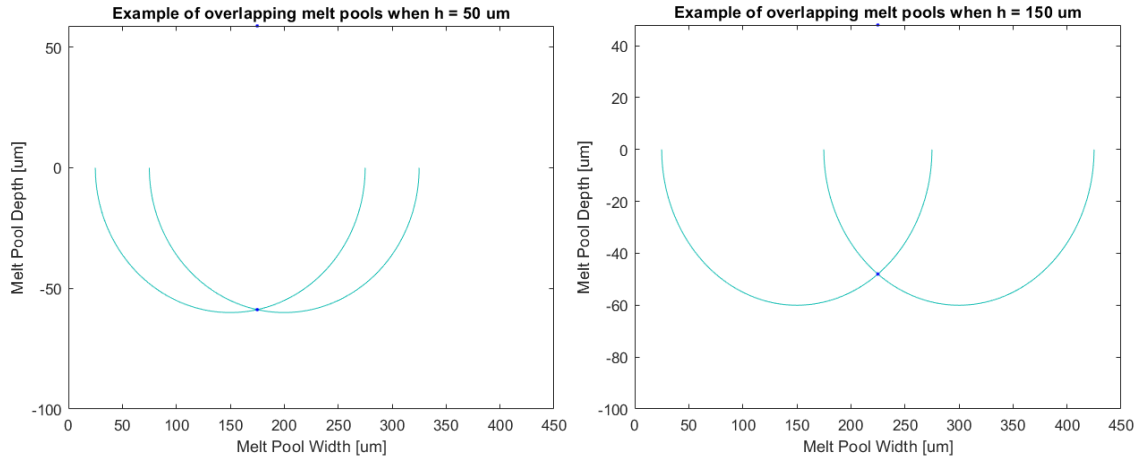

Figure 10. An example of two overlapping melt pools when h = 50 µm (left) and when h = 150 µm (right). The intersecting points (t_{max}) are 58 and 48 µm, respectively.

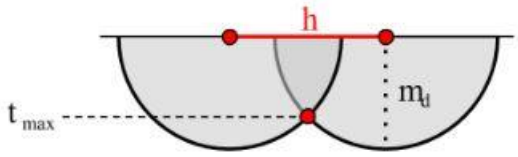

Figure 11. Simplified schematic showing two overlapping melt pools with labeled h, M_d and t_{max}.

Similar to the previous three process parameters (P, v, and t), h also has theoretical and functional constraints. The theoretical minimum h is 0 (single-track experiments). The theoretical maximum is twice the width of the melt pool which would ultimately produce a t_{max} value of 0 µmand display maximum LOF between melt pools. In functional terms, the minimum h should not be less than half the width of the melt pool. The maximum h should produce a t_{max} value the is at least equal or greater than the layer thickness.

3.8 Print Cubes

Once the process parameters have been optimized, we can begin printing 3D test specimen (e.g., cubes, pillars, thin walls, etc). After test specimen are printed, it is necessary to perform the following experiments:

- Measure the density and porosity of the cubes using the Archimedes method.
- Cut cross sections of the cubes and quantify elemental loss using wavelength dispersive spectroscopy (WDS).[5]

[5] Details on how we cut the cross sections of the cubes are outlined in *Chapter 4: Experimental Methods*.

- Perform microstructural analysis using secondary electron microscopy (SEM) and backscatter electron microscopy (BSE).

3.9 Determine Mechanical Properties of New Material

The final step in in the guideline is to perform mechanical testing. Several mechanical tests can be conducted included tensile, compression, hardness, and fatigue testing. Test specimen are fabricated using the highest density parameters achieved in Step 8. Step 9 finalizes our process-structure-property roadmap for any new material.[6]

[6] Details on the dimensions of the tensile tests are included in *Chapter 4: Experimental Methods*.

CHAPTER IV
EXPERIMENTAL METHODS

4.1 Material Investigated

Gas atomized $NiNb_5$ powder (<100 mesh) produced by Nanoval (Germany) was used for this study. The average particle size is d_{50} = 19.8 μm where d_{xx} denotes the cumulative size percentile of particles that have diameters equal to the number provided. The raw powder was characterized using an FEI Quanta 600 scanning electron microscope (SEM) and wavelength dispersive spectroscopy (WDS) as shown in **Figure 12** and **Table 8**, respectively. SEM images showed mostly spherical particles as well as some elongated particles. Additionally, the powder showed a textured surface as well as some porosity.

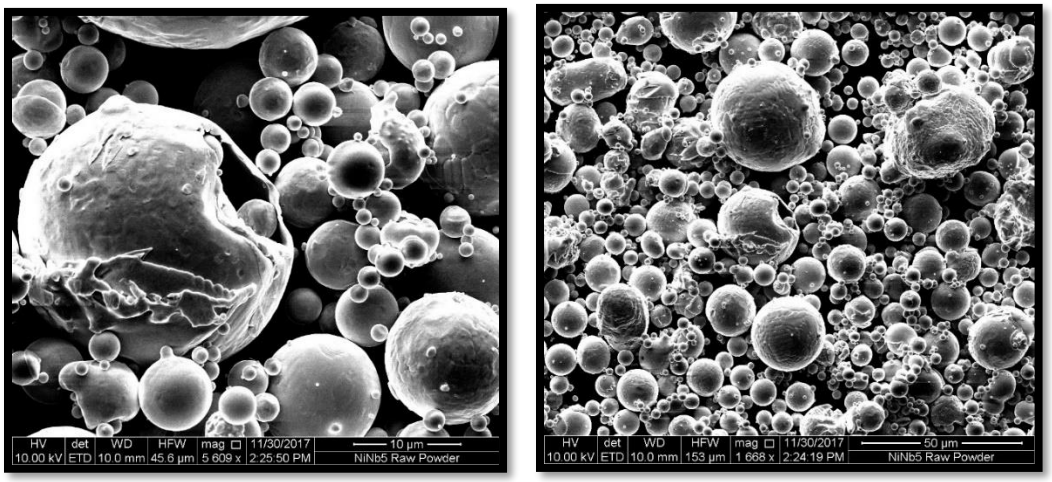

Figure 12. SEM images of raw $NiNb_5$ powder.

Table 7. Chemical composition of raw $NiNb_5$ powder.

Ni	Nb
94.72 (± 0.71)	5.08 (± 0.91)

4.2 Fabrication using LPBF

Experiments are conducted with a 3D Systems ProX 200^{TM} LPBF system, equipped with a fiber laser beam having a Gaussian profile, wavelength λ = 1070 nm, beam spot size of approximately 80 μm in diameter, and a maximum power of 260 W. The experiments were carried out under argon during fabrication.

4.3 Single Track Experiments

4.3.1 Single Tracks: Round One

The purpose of the first set of single track experiments was to validate the dimensions of the melt pool and compare the experimental results with the predictions of the Eagar-Tsai model. Our goal was to test the minimum and maximum power and scan speed boundary conditions for $NiNb_5$. The minimum power was chosen based off the temperature distribution data obtained from the Eagar-Tsai model using the material properties listed in **Table 9.** The melting temperature and density were provided in the Materials Safety Data Sheet (MSDS) provided by the supplier. The thermal conductivity and the specific heat capacity were determined by using the rule of mixtures for the weighted averages of Ni (95%) and Nb (5%). We assumed that absorptivity of pure nickel. A layer thickness of 30 µm was used and a total of 23 single tracks runs were performed on a pure nickel 200 substrate. The power and scan speed combinations are shown in **Figure 13.**

Using the Eagar-Tsai model, we were able to calculate the dimensions and temperature field of the melt pools. The temperature field data showed that a minimum power of 80 W was required to melt the material. A maximum power of 260 W showed temperatures between melting and boiling and thus, it would be expected to observe nickel evaporation in the final builds. Since the

entire melt pool would not be at boiling temperature, we wanted to test the maximum laser power at 260 W. One single track was performed at 55 W to validate if there would be insufficent melting to the substrate.

Table 8. Material properties used for first round of single track experiments.

Thermophysical Property	**Value**	**Reference**
T_m	1703	[70]
k	73	[81]
C_p	506	[81]
η	0.586	[82]
Additional Material Properties		
ρ	8909	[70]

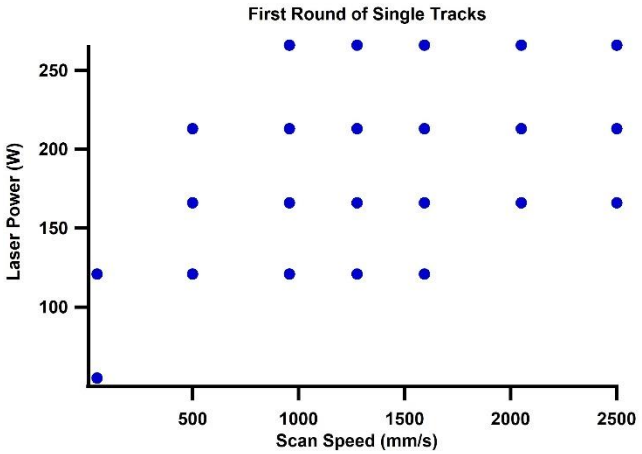

Figure 13. First round of single track runs

Each single track was cut into five cross-sections. The three middle cross sections were mounted in epoxy, polished to silica, and coated with 10 nm gold in preparation for SEM/BSE.

4.3.2 Single Tracks: Round Two

The second set of single track experiments was to again validate the dimensions of the melt pool but with a different set of material properties listed in **Table 10**. Rule of mixtures with values at melting temperature for nickel and niobium was used to determine thermal conductivity and specific heat capacity. Absorptivity was estimated for nickel power. The second round of single tracks had a fixed layer thickness of 30 µm. A total of 40 single tracks runs were performed. The power and scan speed combinations are shown in **Figure 14.**

Table 9. Material properties used for second round of single track experiments

Thermophysical Property	**Value**	**Reference**
T_m	1703	[70]
T_b	3103	[71]
k	70.4	[79]
C	636.19	[83]
η	0.51	[83]
Additional Material Properties		
ρ	8909	[70]

The second round of single tracks were performed on an additively manufactured substrate. The $NiNb_5$ substrate was printed on a nickel 200 substrate with 24 x 60 x 2 mm dimensions and the following parameter settings: 200 W, 750 mm/s, 100 µm hatch spacing, and 35 µm layer thickness. These parameters were chosen so that we could achieve full density. The single tracks were then printed normal to the direction of the scan strategy used for printing the $NiNb_5$ substrate in order to analyze the melt pool dimensions.

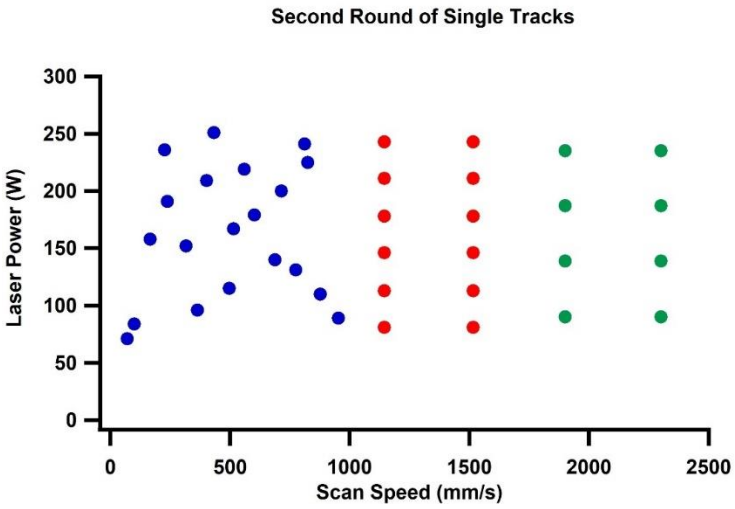

Figure 14. Second round of single track experiments using material properties from Table 10.

4.4 Selecting Parameters for Cubes

Figure 15 was created using the Eagar-Tsai model. The plot shows several important aspects. First, it shows P and v parameters that generate linear energy densities between 0.5 and 2.0 J/mm. The values maximize the design space and allow us to look at a greater range of parameter combinations and their relationship to linear energy density. Furthermore, **Figure 15** shows the range of melt pool depths that can be achieved for various P and v combinations that are the same linear energy density. For instance, a power of 100 W and a speed of 100 mm/s produces a linear energy density of 1.0 J/mm but predicts a M_d than 30 µm. However, the same linear energy density can be achieved with 250 W and 250 mm/s with a predicted M_d value of 69 µm. The points circled in black in **Figure 15** are the cubes we chose for testing. We set the threshold line at melt pool depths of 40 µm. Points above the threshold line are predicted to be successful and points below the line (below 30 µm) are predicted to fail. Each cube was sliced with two cross sections (left and top) as illustrated in **Figure 16.**

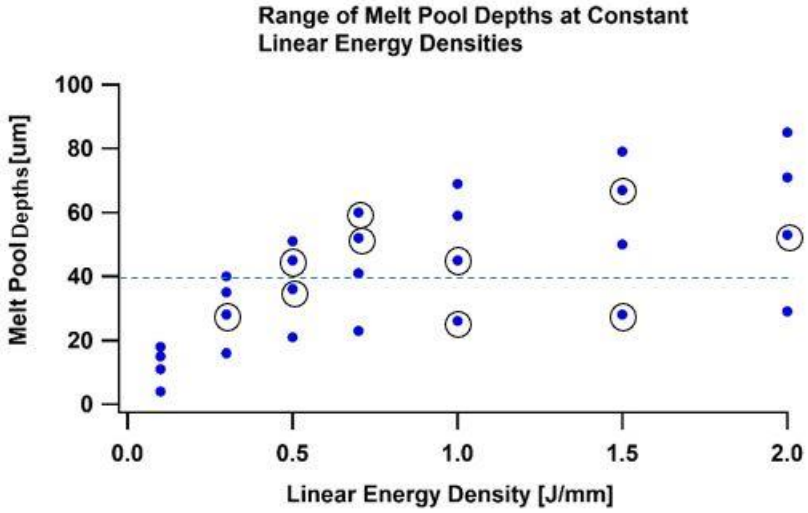

Figure 15. Illustrates the range of melt pool depths that can be achieved for various P and v parameters that produce the same linear energy densities.

4.5 Analysis of Cubes

The porosity and density of the cubes were determined using the Archimedes method. Two cross sections were cut from each cube. One cross section was cut from the left side of the cube in order to analyze features from top to bottom of a build, and the second cross section was taken from the top of the cube. Nickel content was measured using WDS. A total of ten points for each cross section (a total of twenty points for each cube) was taken as shown in **Figure 16**. The average nickel content in wt% is reported in *Chapter 5: Results and Discussion*.

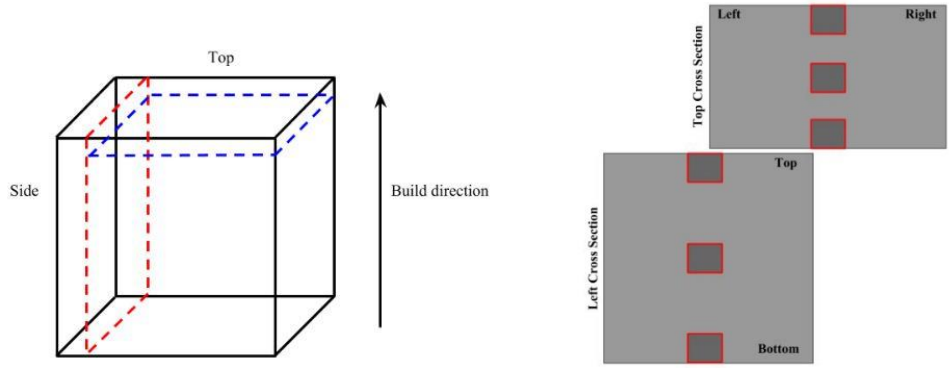

Figure 16. (Left) Side and top cross sections taken from each cube. (Right) Image showing the locations where BSE images were taken on each cross section.

4.6 Mechanical Testing

Five test coupons were fabricated with 34 x 10 x 11 mm^3 dimensions. Tensile specimens with 26 x 7 x 1 mm^3 dimensions were cut from the coupons using a wire electrical discharge machine (EDM). The parameters for each tensile test coupon are listed in **Table 11** and all had a fixed layer thickness of 30 µm. Mechanical tests were performed using an MTS test frame with an MTS extensometer to record strain values.

Table 10. List of tension samples and their corresponding processing parameter combinations.

Sample No.	Power (W)	Scan Speed (mm/s)	Hatch Distance (µm)
1	150	495	85
2	250	825	75
3	100	300	70
4	150	550	75
5	200	500	75

CHAPTER V
RESULTS AND DISCUSSION

5.1 Results of Single Track Experiments

5.1.1 Single Track Results: Round One

Figure 17 shows a summary of predicted and experimental melt pool widths and depths for each run. Runs 1 and 2 had linear energy densities greater than 1 J/mm while runs 3 – 23 had linear energy densities between 0.05 and 0.45 J/mm. **Figure 18** shows runs 3 – 23 to illustrate the differences between predicted and experimental values for linear energy densities less than 0.5 J/mm. Runs 1 and 2 were excluded from **Figure 17** because run 1 showed LOF and run 2 showed significant keyhole mode.

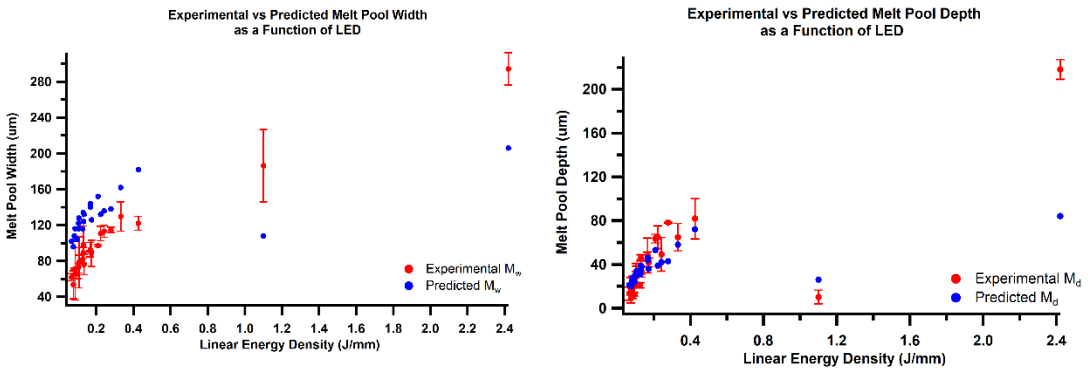

Figure 17. A comparison of predicted and experimental melt pool widths (left) and predicted and experimental melt pool depths (right) for runs 1 – 23 using material properties from Table 9.

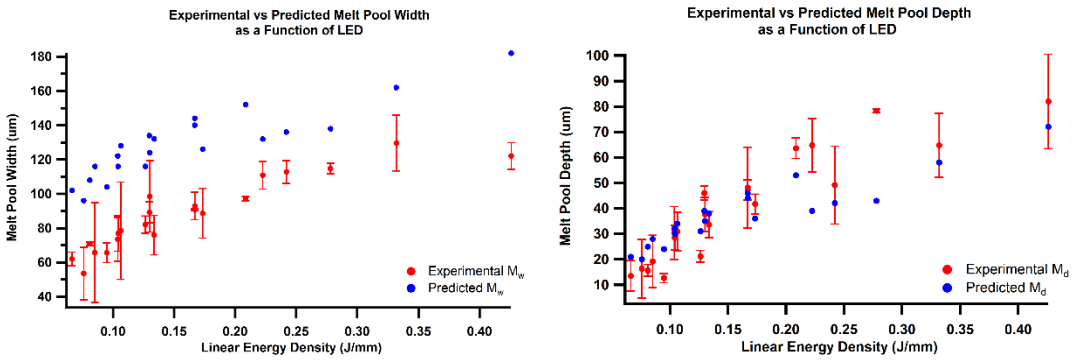

Figure 18. Plots are the same as Figure 4 but exclude runs 1 and 2 to show the comparison between predicted and experimental values at linear energy densities less than 0.5 J/mm.

The BSE images in **Figure 19** show various melt pools for the P and v combinations. The follow series of BSE images show the effect of increasing scan speed at a fixed laser power on melt pool depth. In general, we should see the melt pool depth get smaller, or shallower, as speed increases. We can see that our results agree with this trend. Tracks 1, 6 and 12, for example, show cases where LOF occurs. In other words, cases where the melt pool depth is not sufficient enough to join successive layers. In Track 1, the cause of LOF was due to low laser power. In the remaining tracks, LOF is attributed to too high of a scan speed. Furthermore, Track 10 shows the cross section of a melt pool that is approaching keyhole mode. However, a key feature for identifying keyhole mode is a pore near the tip of the melt pool. Track 9 shows a round feature on the left of the melt pool. This is most likely an unmelted particle because it is approximately 45 µm in diameter with is the maximum particle size of the NiNb powder.

Most of the single tracks in the first round were determined to not have sufficient melt pool depths due to the very high scan speeds. Therefore, a second round of single tracks were tested and the results are discussed in more detail in *Section 5.1.2*.

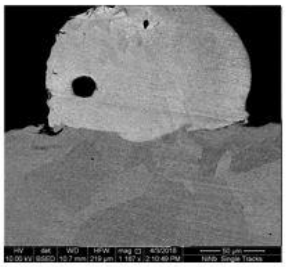

Track 1: 68 W, 50 mm/s

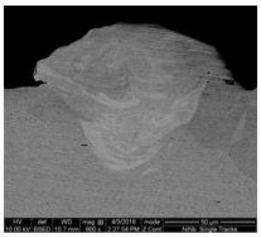

Track 2: 121 W, 50 mm/s

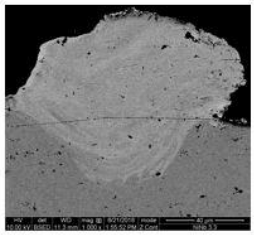

Track 3: 121 W, 500 mm/s

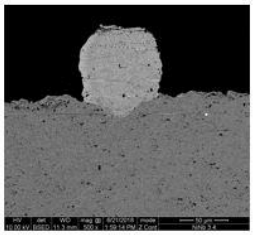

Track 4: 121 W, 957 mm/s

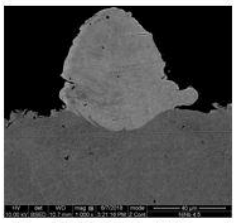

Track 5: 121 W, 1275 mm/s

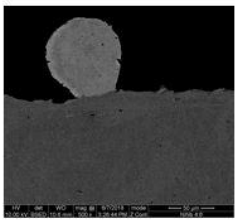

Track 6: 121 W, 1593 mm/s

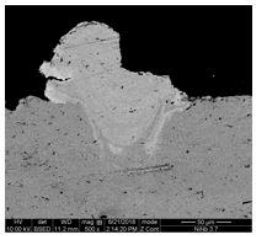

Track 7: 166 W, 500 mm/s

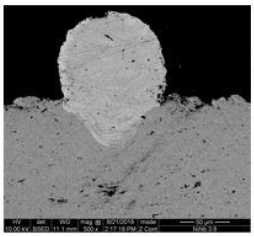

Track 8: 166 W, 957 mm/s

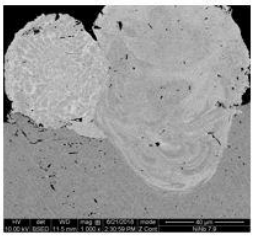

Track 9: 166 W, 1275 mm/s

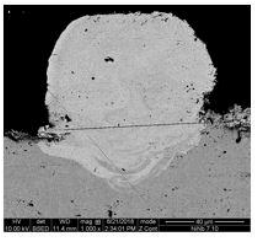

Track 10: 166 W, 1593 mm/s

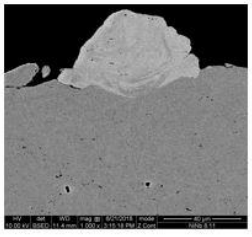

Track 11: 166 W, 2050 mm/s

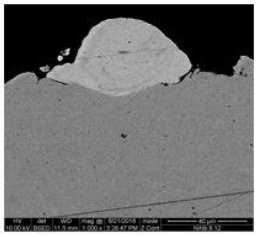

Track 12: 166 W, 2500 mm/s

Figure 19. The above micrographs show the cross-sections of several examples of melt pool geometries we can achieve with various process parameters.

5.1.1.1 Calibrating the Material Properties using a Simple Spreadsheet Method

Using the Eagar-Tsai model, a simple approach was used calibrate three material properties: thermal conductivity, specific heat capacity, and absorptivity. **Table 12** shows the lower and upper bounds of each material property and the steps used to test each property. First, a single material property was changed as the other properties were fixed. The resulting melt pool widths and depths were recorded, and a trend was identified. For instance, as the value of thermal conductivity increased, the melt pool width and depth would decrease. Similarly, as heat capacity increased, the width and depth decreased. The opposing trend is seen for absorptivity. As absorptivity is increased, the melt pool dimensions also increase. Using a spreadsheet, the melt pool width and depth values were recorded with each change in material property until the melt pool width prediction aligned with the experimental values.

The M_w was overpredicted by an average of 42 µm while the M_d was underpredicted by an average of 2.5 µm. It is reasonable that the M_w was overpredicted because the Eagar-Tsai model does not assume there to be a layer of powder, but instead, a solid material. According to previous studies, the powder acts as a thermal insulator and consequently, has lower thermal conductivity than the solid substrate underneath (8). Because of the solid-powder conductivity differences, the heat transfer effects on the M_w are more significant in single track experiments than in multi-layer builds, thus creating narrower M_w than predicted and as illustrated in **Figures 17** and **18**. For this reason, we calibrated the Eagar-Tsai material properties to better match the experimental M_w. However, as we calibrated the melt pool width, the melt pool depth values were shifted to underpredict as illustrated in **Figure 20**. For multi-layer builds, we would expect to see melt pool

depths between the experimental values (upper bound) and the new calibrated values (lower bound).

Table 11. Calibration of material properties for first round of single tracks.

Material Property	Lower Bound	Upper Bound	Step
Thermal Conductivity	63	83	5
Specific Heat Capacity	456	556	25
Absorptivity	0.486	0.686	0.1

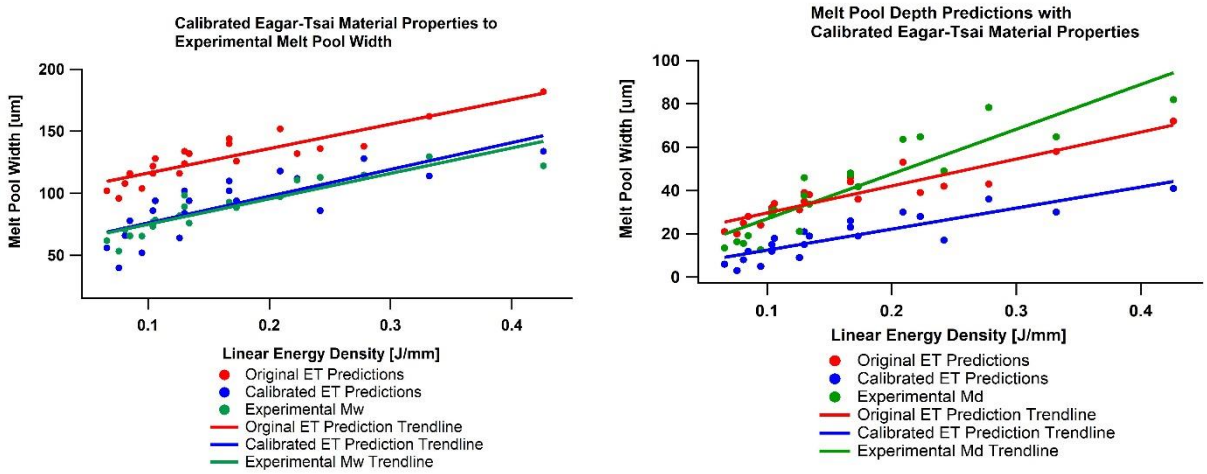

Figure 20. Plot on the left shows the original predictions, new predications using the calibrated material properties, and the experimental values for melt pool width. The plot of the right shows the same scheme for calibrated melt pool depths.

Table 12. Calibrated material properties for first round single tracks.

Material Property	Thermal Conductivity	Specific Heat Capacity	Absorptivity
Value	83	556	0.366

Since the calibrated M_d values become our lower bound values, we can make decisions based off the Eagar-Tsai model predictions that generate depths greater than 40 µm and know that we are in a conservative region for multi-layer builds.

5.1.2 Single Track Results: Round Two

Figure 21 shows a summary of the predicted and experimental melt pool widths and depths using the material properties in **Table 10**. The melt pool widths are overpredicted at lower LEDs and underpredicted at LEDs greater than 0.7 J/mm. The melt pool depths greatly underpredicted. Our focus this round was to be able to predict the melt pool widths with greater accuracy to reduce time in measuring the widths and depths in the cross sections. We also wanted to be able to classify good runs and bad runs based on the observations of the top view of the single tracks as shown in the SEM images in **Figure 22**. The corresponding cross sections of the runs shown in **Figure 22** are shown in **Figure 23**. The cross sections were etched and analyzed under an optical microscope.

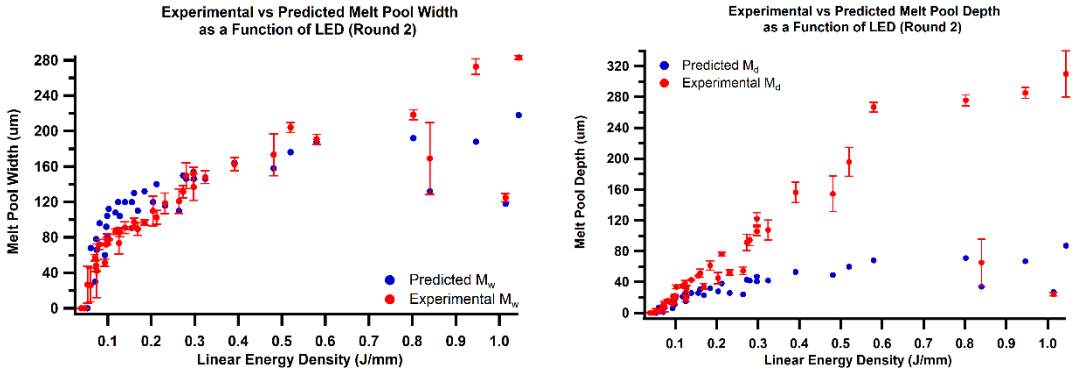

Figure 21. A comparison of experimental and predicted melt pool widths and depths for the second round of single track experiments.

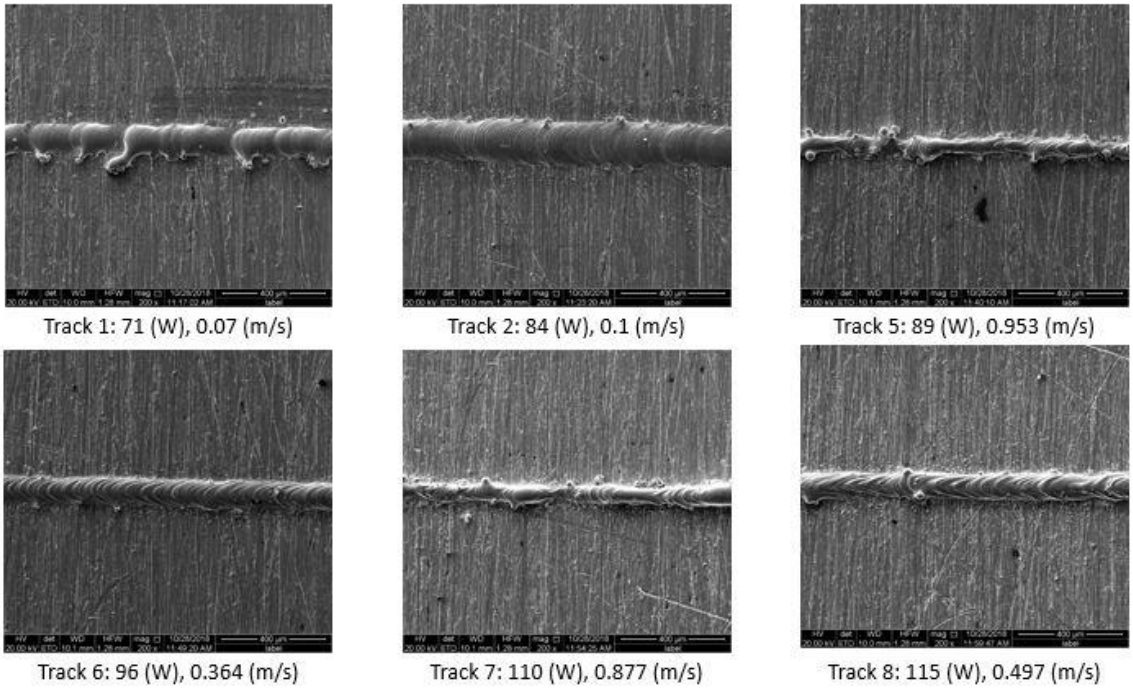

Figure 22. The SEM images show the top view of several second round of single tracks.

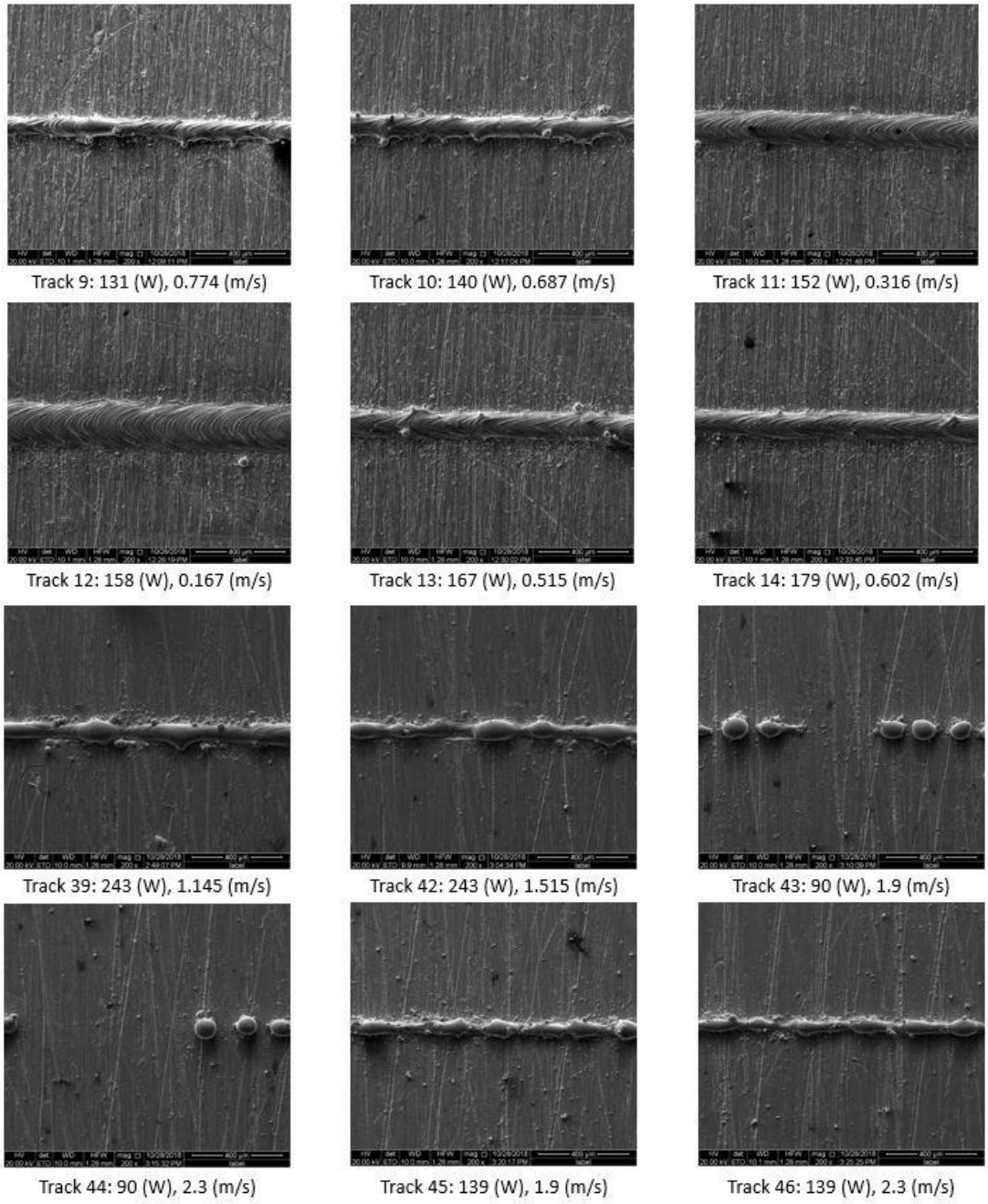

Figure 22, Continued. The SEM images show the top view of several second round of single tracks.

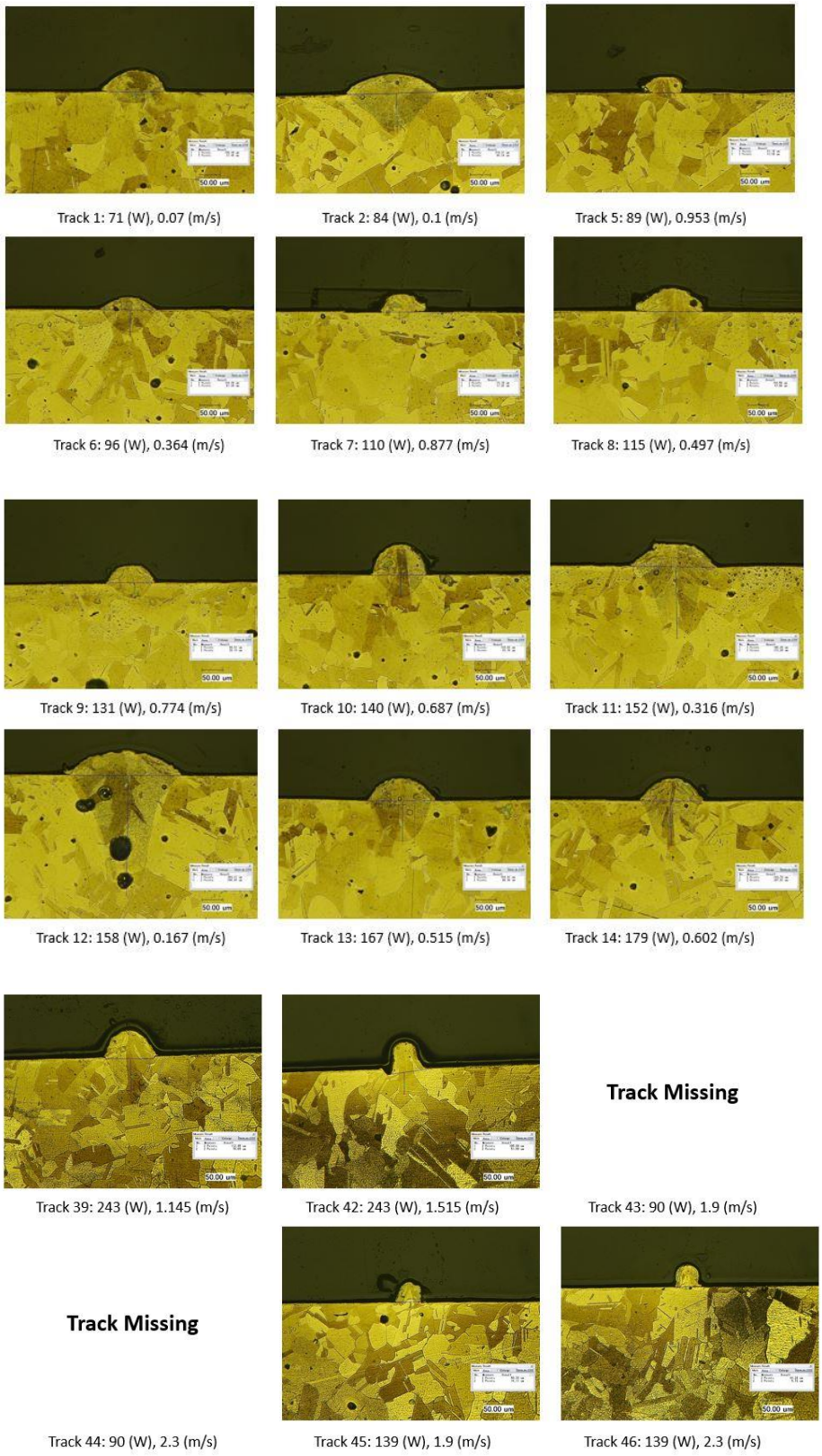

Figure 23. The optical images above show the cross-section of the runs in **Figure 22**.

Looking at the top of the single tracks, a good run can simply be classified as a run where the track is continuous and shows little variation in width along the length of the track. Tracks 6, 11, and 12 are good examples of continuous tracks. Tracks 1, 5, and 46 are examples of inconsistent tracks but are not cases where balling occurs. Balling is where the scan speed is too high for the given laser power and begins to skip across the surface creating gaps of unmelted regions of powder as observed in Tracks 43 and 44.

Based off the top view of the single tracks, we can quickly eliminate process parameters where balling occurs (e.g., Tracks 39 – 44). If we were to classify Tracks 2, 6, 8, and 9 -14 as good runs based off the top view, then we would need to verify by analyzing the melt pool depth in the cross sections of those tracks. The tracks that we classified as good runs based on the top view had depths greater than 30 μm which implies that we would get sufficient bonding with successive layers. However, some tracks showed keyholing such as Track 12. The depth was measured to be 285.45 μm and the cross section should cavities near the top of the melt pool clearly indicating that the process parameters were in the keyhole region. The width of Track 12 was 218.24 μm while the widths of the other "good run" tracks were approximately between 90 and 170 μm. Tracks 15 and 19 (not shown) also had widths and depths greater than 200 μm as well porosity due to keyholing. Therefore, if we are trying to classify runs based off the top view and width of the tracks, we could rule out process parameters that give widths greater than 200 μm as be within a conservative region.

Similarly, it is important to verify that tracks we classified as “bad runs” based off the top view due in fact have in sufficient melt pool depths. Let’s look at Tracks 1, 39, and 42 pictured above. Track 1 had a melt pool depth less than 30 µm and thus, would be in the LOF region. However, Tracks 39 and 42 had depths of 72.58 and 48.80 µm, respectively. Since these depths are greater than the layer thickness, we would categorize these as good runs that are sufficient for joining successive layers. However, the widths of those tracks (87.60 and 76.96 µm, respectively) are also very small and close the depth values. These tracks also showed some variability along the length of the track. In the second round of single tracks, runs with depths less than 30 µm had widths less than 100 µm. Therefore, if we wanted to make faster decisions and stay within a conservative region based off the top view of the single tracks, we could eliminate runs with widths less than 100 µm.

5.1.2.1 Calibration of Eagar-Tsai Model

A surrogate model was generated in order to calibrate the second set of single track experiments. This is a more sophisticated approach than the simple spreadsheet method. The benefits of using a surrogate model to perform the calibration is that many trials can be run in a short amount of time. For the surrogate model, three material properties (k, C_p, and η) were calibrated using a range of lower and upper bound values as listed in **Table 14**. Rather than outputting a single, optimal value for each material property, the model outputs the show the probability for a range of material property values as shown in **Figure 24**. Each distribution in **Figure 25** has a peak that indicates the value with the highest probability. In future studies, this calibration range can be narrowed to get a distribution with more distinguishable peak values.

Table 13. Range of material properties tested for Eagar-Tsai model calibration.

Material Property	Lower Bound	Upper Bound	Comments
Thermal Conductivity [W/(m*K)]	40	120	Weighted average of the values for Ni_{95} and Nb_5 at solid and liquid at T_m.
Specific Heat Capacity [J/(kg*K)]	636.19	756.3	Weighted average of the values for Ni_{95} and Nb_5 at melting and at vaporization.
Absorptivity (0 – 1)	0	1	
Total Simulations	*210 Simulations*		

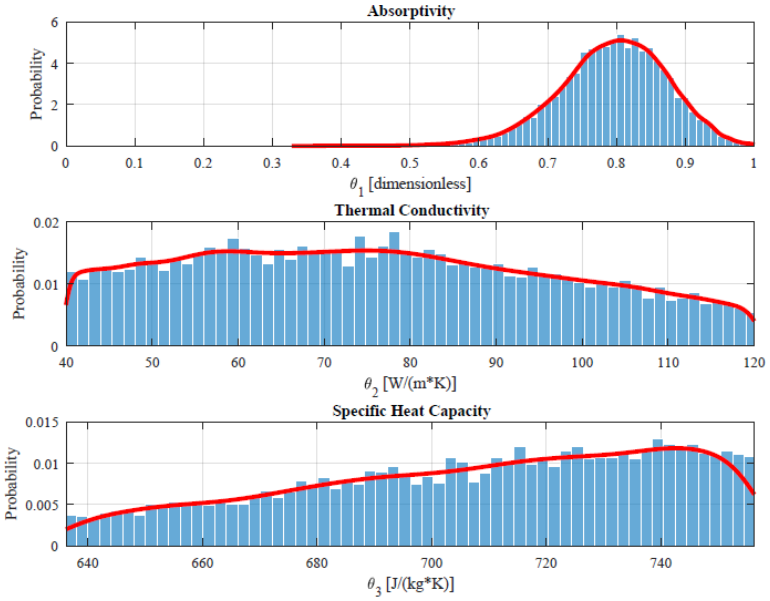

Figure 24. Distribution of the three calibration parameters.

The calibrated values are then cross validated with the experimental values as well as the Multivariate Gaussian Process (MVGP) data as shown in the plot in **Figure 25**. We can observe that the calibrated data aligns very well to the experimental data and thus, we can be confident in the calibrated values for building cubes. To validate the calibrated values, used the Eagar-Tsai

model with the calibrated values for the second round single track experiments and compared to the uncalibrated widths predications as well as the experimental values. A comparison of these values is shown in **Figure 26**. Before calibrating the model, we were overpredicting melt pool widths and we can see that the calibrated values match well with the experimental values at lower LED and slightly underpredict at moderate LED. At LED greater than 0.7 J/mm, the original and calibrated material properties do not predict melt pool widths with accuracy. This is most likely because we are in keyhole mode (very large melt pool depths) and the Eagar-Tsai model cannot predict keyholing.

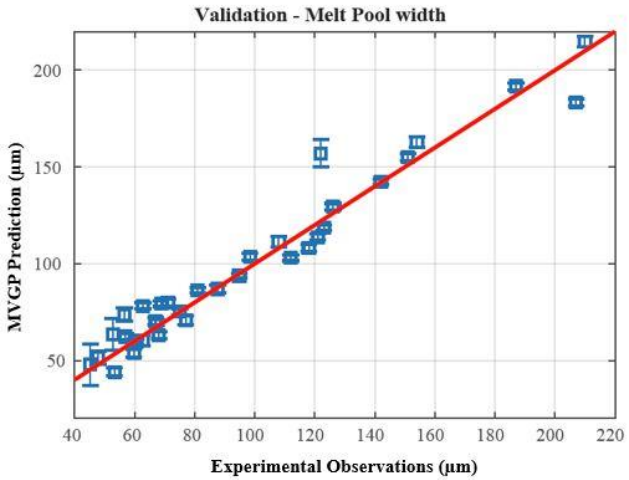

Figure 25. Cross validation of the calibration results
with the experimental and multivariate Gaussian Process Data.

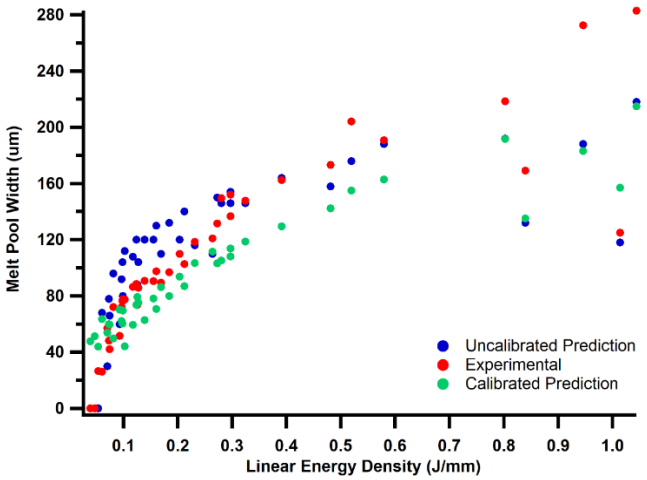

Figure 26. A comparison of uncalibrated, calibrated, and experimental melt pool widths as a function of LED.

5.2 Analysis of Cubes

The follow two sets of cubes were built based off the first round of single tracks and **Figure 15** presented in *Chapter 4: Experimental Methods* section.[7]

5.2.1 Cubes Set 1

After calibrating the Eagar-Tsai model material properties to the melt pool widths, the predicted melt pool depths shift below the experimental values as discussed in *Section 5.1.1.1*. However, based on the concepts from Mukherjee *et al.*, we expect to see the depths in successive layers to become slightly smaller than the single track values. Therefore, the experimental trendline becomes the upper boundary condition and the new calibrated predicted melt pool depths become the lower boundary condition (**Figure 20**). The first set of cubes tests to see if we are closer to the experimental trendline or the calibrated ET trendline. Values were chosen so that we explored

[7] The surrogate model was not available until later studies. The predicted melt pool depths values shown in **Table 15** were added later and are not the same values shown in **Figure 14**. The values in **Table 15** are more accurate.

a new design space (linear energy densities between 0.3 – 1.5 J/mm). We looked at a range of M_d at constant LED. Since these values are based off Eagar-Tsai predications, those values are considered "lower bound." We looked for 6 values above 40 µm and four values below 30 µm. The six values above 40 should be the successful runs and the four under 30 should produce LOF and therefore, fail. A list of parameters used for Set 1 is summarized in **Table 15**. The successful and failed builds are shown in **Figure 27**.

Table 14. First set of cubes with various P and v conditions with a constant h at 50 µm.

Cube No.	Power (W)	Speed (mm/s)	Predicted M_d (µm)	Volumetric Energy Density (J/mm^3)	Density (%)	Porosity (%)
1a	150	495	38	202.020	98.141	1.859
2a	150	300	50	333.333	95.545	4.465
3a	200	400	58	333.333	96.173	3.827
4a	200	280	69	476.190	Fail	Fail
5a	250	350	76	476.190	Fail	Fail
6a	100	100	45	666.667	97.188	2.812
7a	150	150	66	666.667	93.966	6.034
8a	100	65	50	1025.641	94.169	5.831
9a	200	130	92	1025.641	Fail	Fail
10a	150	75	81	1333.333	Fail	Fail

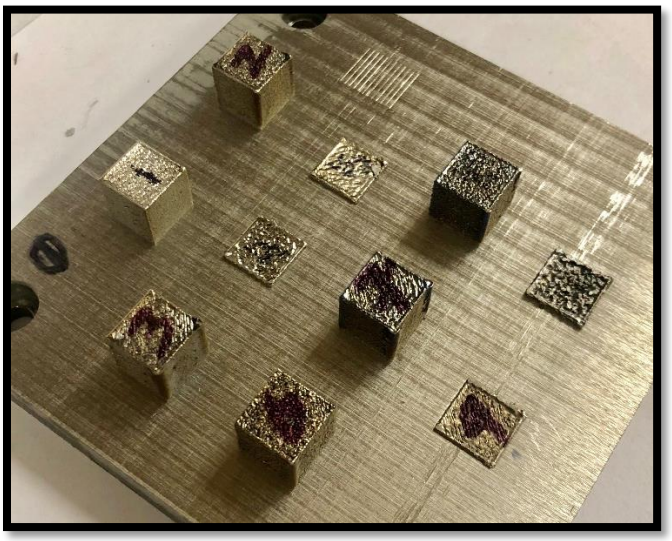

Figure 27. Image showing final build of first set of cubes.

Figure 28 shows BSE images for the side and top cross sections of cubes 1a, 2a, and 7a. These samples were fabricated with the same P, h, and t process parameters but vary with scan speed. As scan speed increases, we observe a decrease in porosity. Similar observations were seen in SLM fabricated nickel components [68]. The porosity features also vary in size and geometry. Cube 1a had porosity concentrated toward the bottom of the build. The elongated imperfections seen in the "Cube 1a: Left Bottom" BSE image were an average of 11.8 µm. This type of porosity is most likely due to LOF. As heat accumulates throughout the build process and successive layers are remelted and reheated, the porosity and LOF imperfections decrease. In the "Left Bottom" BSE images of cubes 2a and 7a, the average size of the porosity features were 29.17 and 54.04, respectively. As the size of the porosity increased, the overall density of the build decreased. The large, elongated defect seen in "Cube 1a: Top Right" may be attributed to the fact that is was part of the final sintered region of the build and could have undergone shrinkage upon solidification.

In other words, the final top layers of the build are not remelted and reheated multiple times like the layers beneath. Additionally, the top layers experience more convective heat transfer than conductive heat transfer, leading to possible shrinkage and defect issues.

As mentioned before, builds with the same LED (or VED) with various process parameters will not produce the same melt pool geometry. Cubes 6a and 7a have the same VED however, Cube 7a is approaching the keyholing region and therefore, there is a greater tendency to produce cavities (i.e., porosity). The predicted melt pool depth column was added after later studies. The predicted M_d values are based off the calibrated parameters from the surrogate model, giving us better accuracy as to what we are observing. We can clearly see that the four cubes that failed to print were well into the keyholing region.

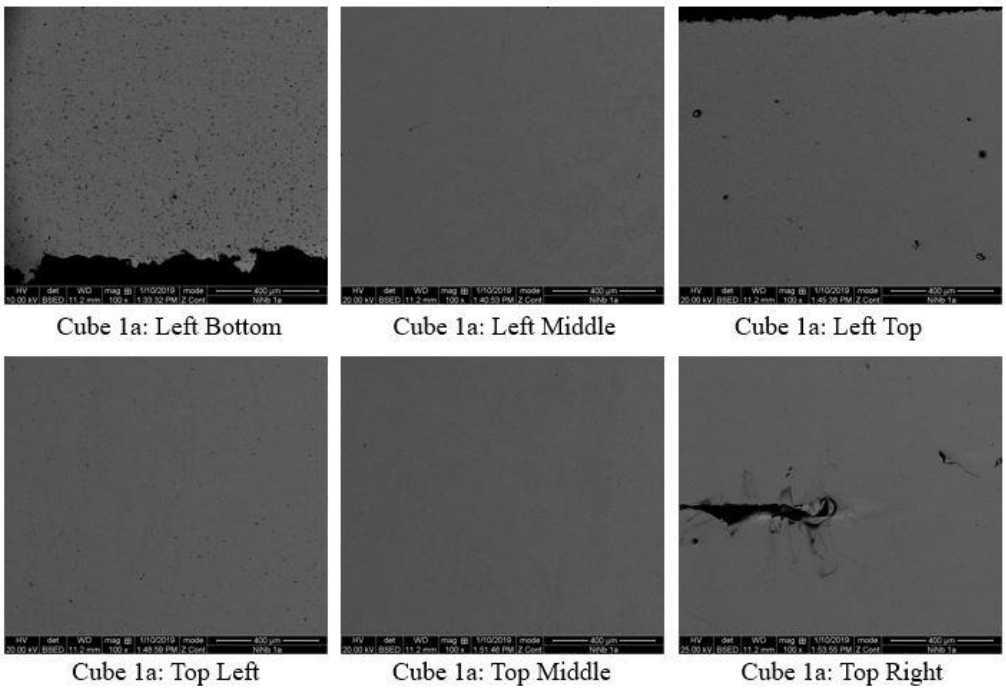

Figure 28. The BSE images above showcase various
levels of porosity achieved with different process parameters

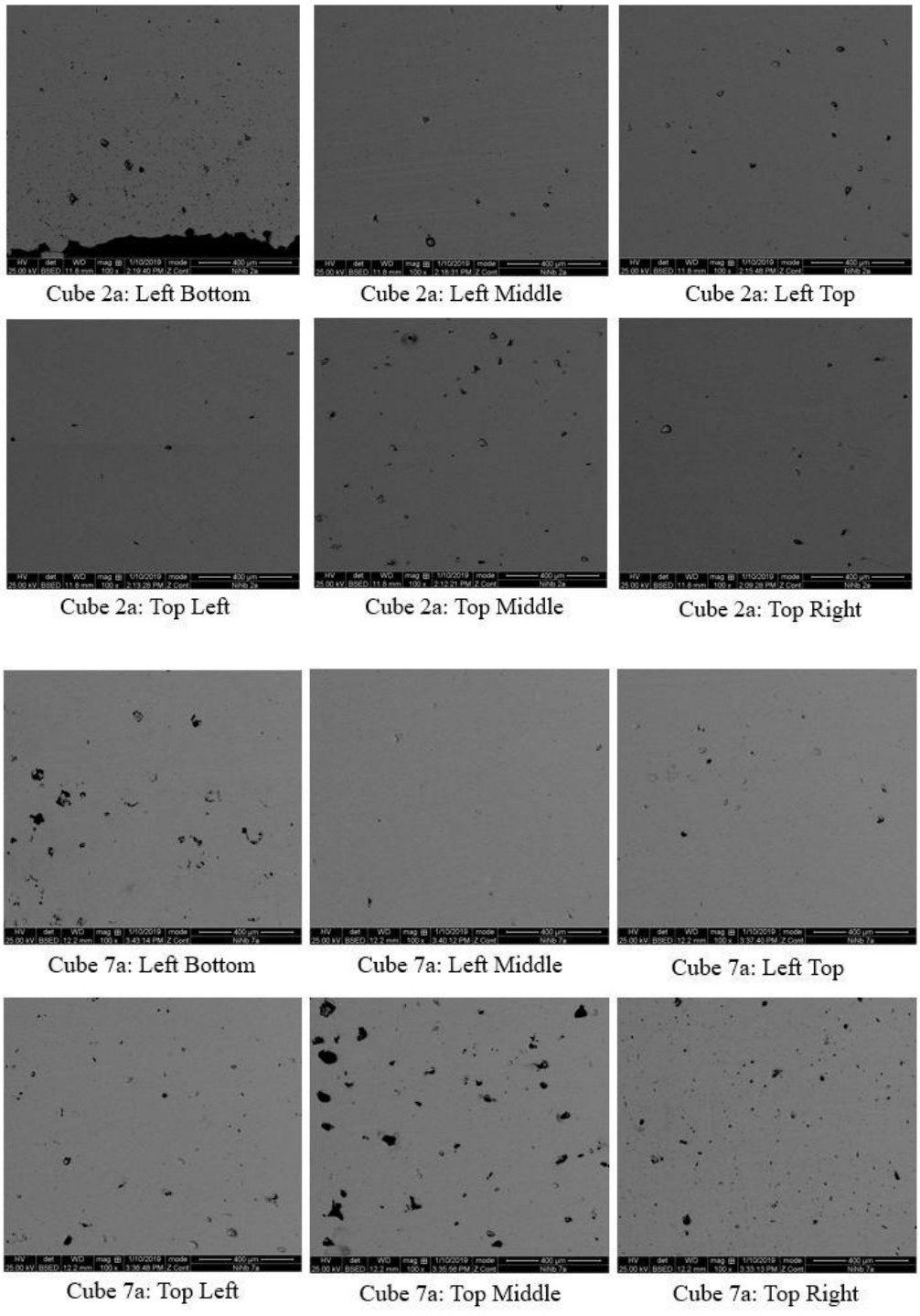

Figure 28, Continued. The BSE images above showcase various levels of porosity achieved with different process parameters.

5.2.2 Cubes Set 2

Next, we wanted to see if we could determine the optimal hatch distance for builds. We chose two P and v combinations and tested each with five h values as listed in **Table 16**. Five h values were chosen for each P and v combination. Two h values were calculated so that the melt pool overlap distance t_{max} would be greater than 30 µm ensuring a successful build. Cubes 1b, 2b, 6b, and 7b have conservative hatch distances. These cubes are predicted to be successful and produce the highest density builds because the layer thickness is set to 30 µm. If t_{max} is greater than 30 µm then we should not get LOF. An h value that produced a t_{max} value of 30 µm was also chosen (Cubes 3b and 8b). This cube should not fail but we should see some LOF in some areas due to the variation in the melt pool depth along the length of the scan path. Two h values were chosen so that t_{max} would be less than 30 µm and produce LOF and thus produce lower density parts (Cubes 4b, 5b, 9b and 10b). The final build of the second set of cubes is shown in **Figure 29**.

Table 15. Second set of cubes with constant P and v and various hatch spacings

Cube No.	Power (W)	Speed (mm/s)	Hatch Spacing (µm)	Volumetric Energy Density (J/mm^3)	Density (%)	Porosity (%)
1b	250	825	115	168.350	99.756	0.244
2b	250	825	105	134.680	99.927	0.073
3b	250	825	85	118.835	99.701	0.299
4b	250	825	75	96.200	99.762	0.238
5b	250	825	60	87.835	99.892	0.108
6b	150	495	85	118.835	99.743	0.257
7b	150	495	120	84.175	99.376	0.624
8b	150	495	140	72.150	97.883	2.117
9b	150	495	150	67.340	96.425	3.575
10b	150	495	155	65.168	96.376	3.624

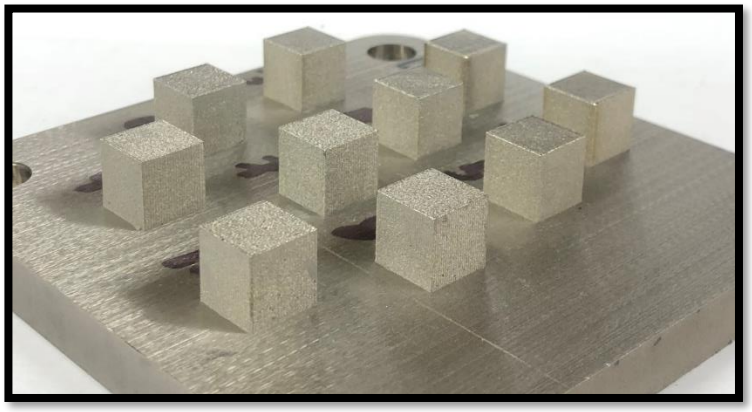

Figure 29. Image of final build of second set of cubes.

Figure 30 shows cube 1b with very little porosity defects throughout the build. Using the calibrated material property values, the Eagar-Tsai model predicted the melt poo depths in Cubes 1b – 5b and Cubes 6b – 10b to be 48 µm and 387 µm, respectively. Cubes 6b – 10b match with what we originally predicted. Cubes 6b and 7b had the greatest density (i.e., lowest porosity) which is what we predicted when calculating h and determining t_{max} to be greater than 30 µm. Cube 8b has greater porosity than the previous cubes but less than Cubes 9b and 10b. This also matches with what we expect because we calculated the h value to give a t_{max} equal to 30 µm. Finally, Cubes 9b and 10b give the lowest density builds (i.e., highest porosity) of the five for this P and v combination. These cubes were fabricated with an h value that produced a t_{max} less than 30 µm.

Cubes 1b – 5b did not give the same trends as we predicted in Cubes 6b – 10b. The most likely reason is that the melt pool depth was greater and thus, the slight variations in h and t_{max} values were not as sensitive as they were with the parameters in Cubes 6b – 10b that had a predicted melt pool depth of 38 µm. With a predicted melt pool depth of 38 µm, we know that the melt pool

varies along the length of the path and thus, has a greater likelihood of producing LOF. A summary of the density as a function of hatch distance for the second set of cubes is shown in **Figure 32**.

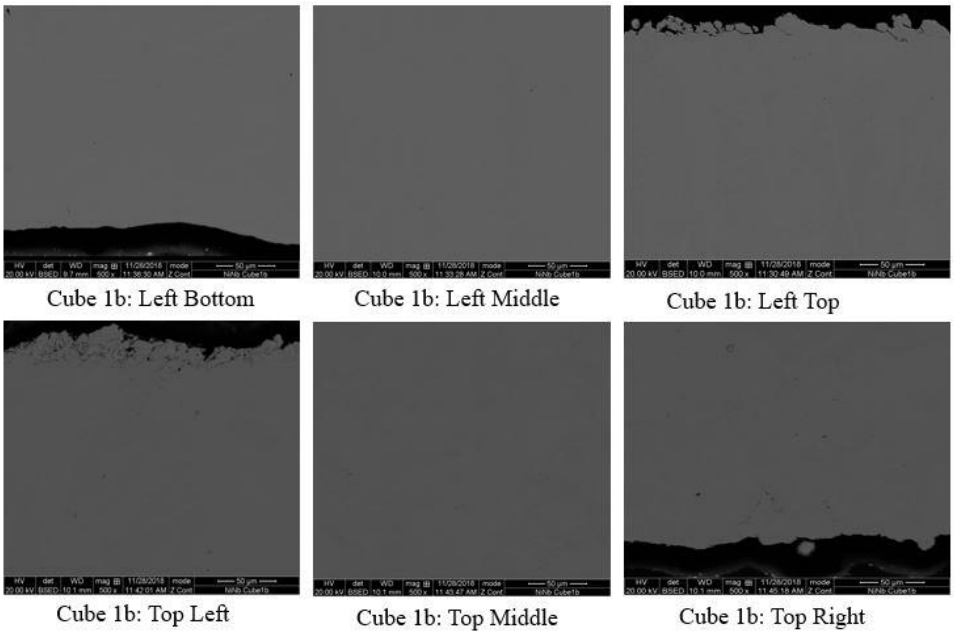

Figure 30. The BSE images above show cube 1b (99.756%).

5.2.3 Porosity and Density Analysis

When porosity as a function of volumetric energy density (VED) is plotted, we see that builds with less than 2 percent porosity were between 80 and 200 J/mm^3. Builds that had less than 1 percent porosity were between 87 and 168 J/mm^3 (**Figure 31**). This became the region of focus for choosing process parameters to build tensile samples. This is discussed in more detail in *Section 5.4*.

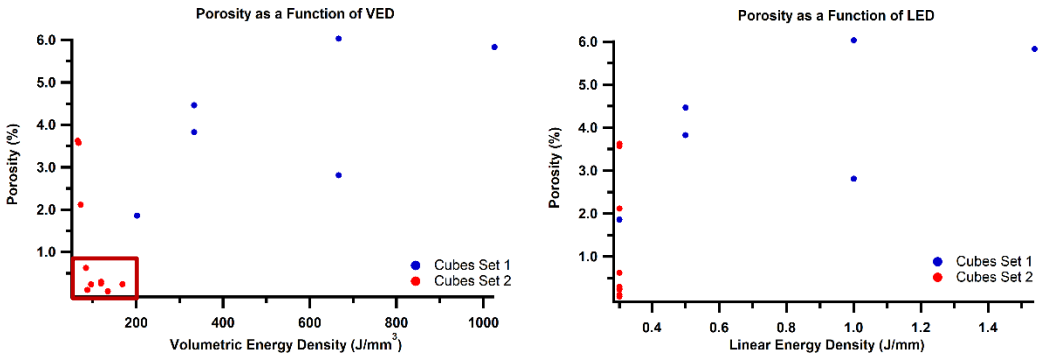

Figure 31. Plot showing the relationship between volumetric energy density (VED) and the porosity of the builds for sets 1 and 2.

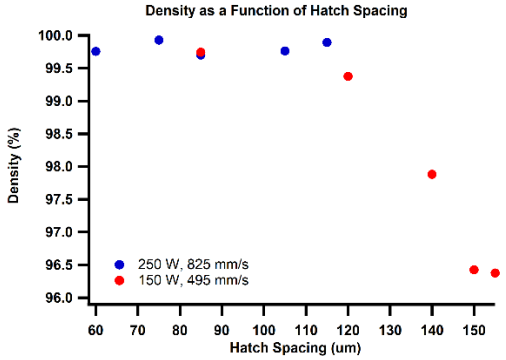

Figure 32. Plot showing density as a function of hatch spacing for second set of cubes.

5.3 Differential Evaporation of Nickel

We wanted to investigate the evaporation of nickel as function of process parameters and volumetric energy density. The left cross section and top cross sections of each cube were compared for analysis to determine if greater nickel evaporation was observed at the top of the cube versus the bottom and mid-sections of the build. As we expect, the top cross sections of the cubes showed a greater amount of nickel loss compared to the side section. This can be explained by the greater amount of heat accumulated at the top of the build. Furthermore, we observe greater

differential evaporation of nickel at VEDs greater than 200 J/mm^3 compared to builds between 90 and 200 J/mm^3.

Cubes from set 1 had a greater range of VED. Recall that Set 1 had constant h and t and varying P and v process parameters. Set 1 is highlighted in blue in both plots in **Figure 33**. Only the first five cubes of set two were analyzed. Cubes 6 -10 of set 2 had the same P and v parameters from cube 1a in set 1. Cubes 6b – 10b only varied in hatch distance and thus, we anticipated that the nickel content would be close to cube 1a. Set 2 is highlighted in red in both plots in **Figure 33** . Set 2 varied in VED between 90 and 200 J/mm^3. Cubes 1b – 5b had constant P, v, and t parameters while h varied. There was no clear trend in nickel evaporation as a function of hatch distance.

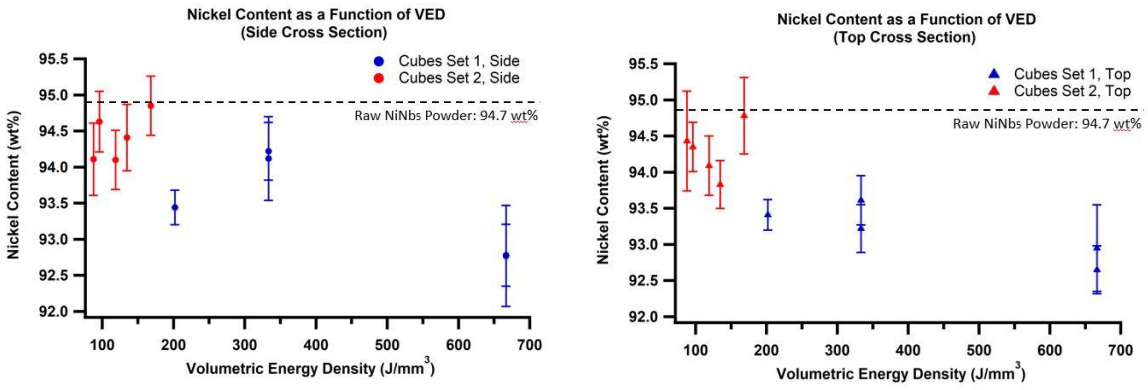

Figure 33. Plots illustrating nickel content as a function of VED for the left and top cross sections of the printed cubes.

5.4 Mechanical Properties

The first two tensile samples were based on the best two cube prints listed in **Table 16** (cube 6b and 1b, for tensile samples 1 and 2, respectively). The remaining three tensile sample parameters were chosen based on the porosity data plotted as a function of VED. The data showed that low

porosity builds were in the range of 80 to 200 J/mm^3. Process parameters yielding VED between 118 and 177 J/mm^3 were chosen for the last three tension samples as listed in **Table 17**. Tension data for samples 1 through 5 are shown in **Figure 34**. Yap *et al.* reported that SLM-processed pure nickel achieved an ultimate tensile strength (UTS) of 452.0 ± 7.4 MPa and a yield strength (YS) of 240.3 ± 14.0 MPa [68]. It is found that LPBF-processed $NiNb_5$ has a higher tensile strength and yield strength than pure nickel and SLM-processed pure nickel. Furthermore, LPBF-processed $NiNb_5$ has slightly greater ductility that SLM-processed pure nickel.

Table 16. Tensile test specimen parameters

Sample	**150 W, 495 mm/s, h = 85 µm**	**250 W, 825 mm/s, h = 75 µm**	**100 W, 300 mm/s, h = 70 µm**	**150 W, 550 mm/s, h = 75 µm**	**200 W, 500 mm/s, h = 75 µm**
VED (J/mm^3)	118.835	134.680	158.730	121.212	177.778
Yield Strength (MPa)	~ 610	~610	~600	~600	~600
Ultimate Tensile Strength (MPa)	~720	~775	~720	~750	~750
Elongation (%)	13	16	15	13	16

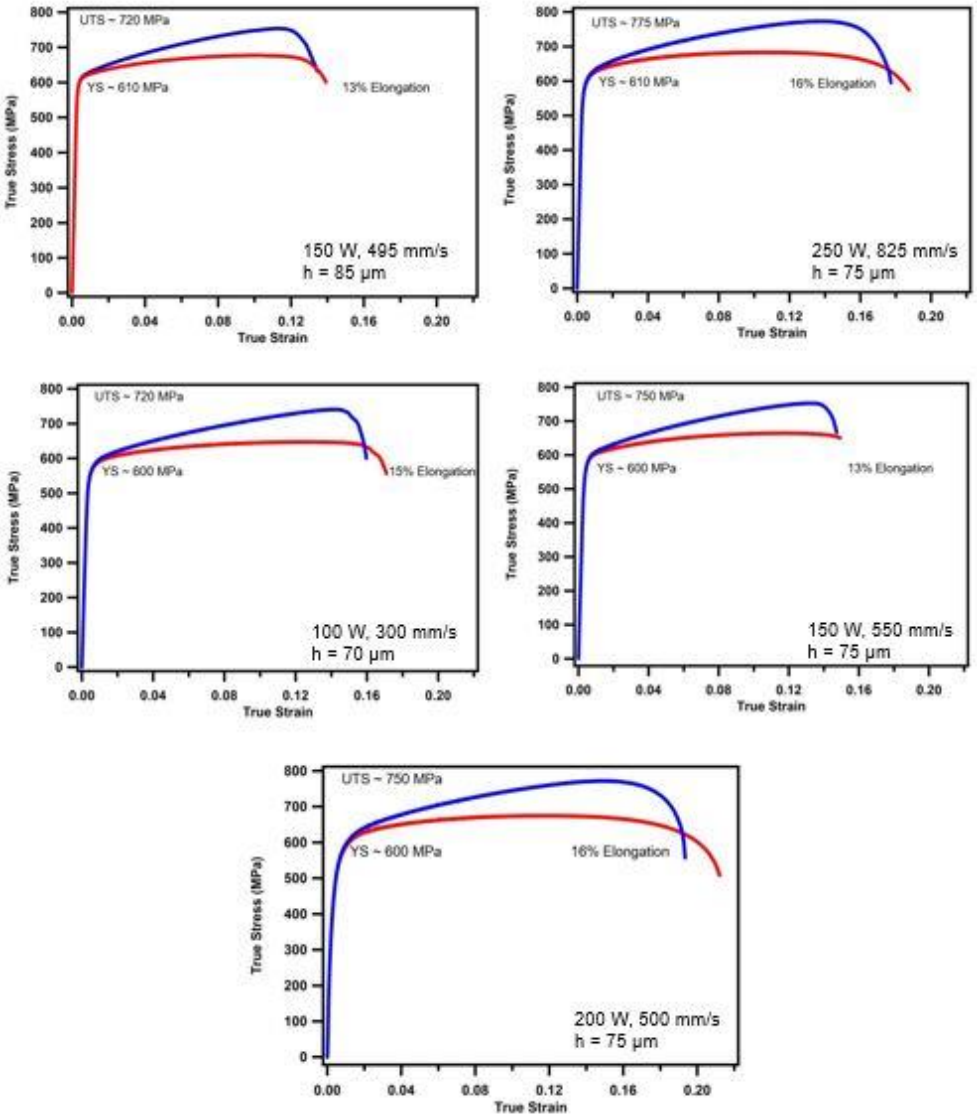

Figure 34. Plots showing tension data for each of the five samples.

CHAPTER VI
CONCLUSION AND RECOMMENDATIONS FOR FUTURE WORK

6.1 Conclusion

This work contributes a simple and effective process parameter selection framework for new AM materials. Although more accurate computational models are being developed, they are often costly and require long times. By utilizing a simplified heat transfer model, we can gain a fundamental understanding of the process parameter region of interest for a new material. We have also developed a systematic way of characterizing single tracks, calibrating the Eagar-Tsai model, and achieving high density parts (> 99%). The following summarizes the key results and contributions of this work:

- defining the process region for a new material,
- standardized methods for measuring the melt pool dimensions,
- achieving near full-density parts, and
- reducing build times by optimizing the hatch distance.

Additionally, we investigated the effects of process parameters on the outcomes of the builds. Lower VEDs between 100 – 200 J/mm^3 produced the lowest porosity (i.e., high density) parts. There was not a clear distinction of porosity or nickel content loss as function of laser power and scan speed and the two parameters are dependent on one another. However, it was observed that porosity increased as hatch distance increase due to lack of fusion. Furthermore, as expected, we tend to observe greater nickel content loss near the top of the build compared to the bottom and mid-sections of the build.

6.2 Recommendations for Future Work

It is necessary to carry out the steps presented in this guideline on other AM materials. This research group in particular will be working with other binary nickel alloy systems such as NiAl and NiCu. A comparison between the binary nickel alloys will lead to strong evidence to the effects of LPBF on nickel alloys. This framework should also be performed on new AM materials such as high entropy alloys and steels. Additionally, more microstructural analysis and mechanical testing should be conducted to gain a better understanding of the process, structure, and property relationship of new AM materials. Other recommendations for future work include optimization of layer thickness to reduce overall build times.

REFERENCES

[1] Bureau of Economic Analysis, "Value Added by Industry," *November*, 2018. [Online]. Available: https://apps.bea.gov/iTable/iTable.cfm?isuri=1&reqid=51&series=q&step=51&table_list=1. [Accessed: 31-Dec-2018].

[2] "Bureau of Labor Statistics Data," *November*, 2018. [Online]. Available: https://data.bls.gov/timeseries/CES3000000001?amp%253bdata_tool=XGtable&output_view=data&include_graphs=true. [Accessed: 31-Dec-2018].

[3] T. Manufacturing, "The jobs are here, but where are the people?," *Manuf. Inst.*, 2018.

[4] W. Associates, *Wohlers Report 2018: 3D Printing and Additive manufacturing State of the Industry Annual Worldwide Progress Report*. Fot Collins, Colorado, 2018.

[5] T. DebRoy *et al.*, "Additive manufacturing of metallic components – Process, structure and properties," *Progress in Materials Science*, vol. 92. pp. 112–224, 2018.

[6] T. Mukherjee, J. S. Zuback, A. De, and T. DebRoy, "Printability of alloys for additive manufacturing," *Sci. Rep.*, vol. 6, pp. 1–8, 2016.

[7] M. M. Cotteleer and B. Sniderman, "Forces of change: Industry 4.0," *Deloitte Insights*, 2017.

[8] A. Parrott and W. Lane, "Industry 4.0 and the digital twin," *Deloitte Univ. Press*, pp. 1–17, 2017.

[9] Additive Manufacturing Standardization Collaborative, "Standardization Roadmap for Additive Manufacturing, version 2," no. June, p. 269, 2018.

[10] T. DebRoy *et al.*, "Additive manufacturing of metallic components – Process, structure and properties," *Prog. Mater. Sci.*, vol. 92, pp. 112–224, 2018.

[11] B. Tilton, E. Dobner, and J. Holdowsky, “3D opportunity for standards.,” *Deloitte Insights*, no. November, 2017.

[12] S. D. DuPont, J.N., Lippold, J.C., Kiser, *Welding Metallurgy and Weldability of Nickel-base Alloys*. John Wiley and songs, Inc., 2009.

[13] I. Yadroitsev, P. Krakhmalev, and I. Yadroitsava, “Hierarchical design principles of selective laser melting for high quality metallic objects,” *Addit. Manuf.*, vol. 7, pp. 45–56, 2015.

[14] C. Meier, R. W. Penny, Y. Zou, J. S. Gibbs, and A. J. Hart, “Thermophysical Phenomena in Metal Additive Manufacturing by Selective Laser Melting: Fundamentals, Modeling, Simulation and Experimentation,” 2017.

[15] E. Herderick, “Additive manufacturing of metals: a review,” *Mater. Sci. Technol.*, pp. 1413–1425, 2011.

[16] et al. Yap, C.Y., Chua, C.K., Dong, Z.L., Liu, Z.H., Zhang, D.Q., Loh, L.E., “Review of selective laser melting: Materials and applications,” *Appl Phys Rev*, vol. 2, no. 4, 2015.

[17] M. Lewandowski, J.J., Seifi, “Metal additive manufacturing: a review of mechanical properties,” *Ann Rev Mater Res*, vol. 46, pp. 151–186, 2016.

[18] R. Gu, D.D., Meiners, W., Wissenbach, K., Poprawe, “Laser additive manufacturing of metallic components: materials, processes and mechanisms,” *Int. Mater. Rev.*, vol. 57, no. 3, pp. 133–164, 2012.

[19] H. L. Collins, P.C., Brice, D.A., Samimi, P., Ghamarian, I., Fraser, “Microstructural control of additively manufactured metallic materials,” *Ann Rev Mater Res*, vol. 46, pp. 63–91, 2016.

[20] D. L. Bourell, “Perspectives on additive manufacturing,” *Ann Rev Mater Res*, vol. 46, pp.

1–18, 2016.

[21] et al. King, W.E., Anderson, A.T., Ferencz, R.M., Hodge, N.E., Kamath, C., Khairallah, S.A., “Laser powder bed fusion additive manufacturing of metals; physics, computational, and materials challenges,” *Appl Phys Rev*, vol. 2, no. 4, 2015.

[22] C. Korner, “Additive manufacturing of metallic components by selective electron beam melting - a review,” *Int. Mater. Rev.*, vol. 61, no. 5, pp. 361–377, 2016.

[23] D. Herzog, V. Seyda, E. Wycisk, and C. Emmelmann, “Additive manufacturing of metals,” *Acta Mater.*, vol. 117, pp. 371–392, 2016.

[24] W. J. Sames, F. A. List, S. Pannala, R. R. Dehoff, and S. S. Babu, “The metallurgy and processing science of metal additive manufacturing,” *Int. Mater. Rev.*, vol. 61, no. 5, pp. 315–360, 2016.

[25] W. E. Frazier, “Metal additive manufacturing: A review,” *J. Mater. Eng. Perform.*, vol. 23, no. 6, pp. 1917–1928, 2014.

[26] H. D. Solomon, “Fundamentals of Weld Solidification,” *ASM Handb. Vol. 6, Welding, Brazing, Solder. (ASM Int.*, vol. 6, no. January, pp. 45–54, 1993.

[27] T. Mukherjee, H. L. Wei, A. De, and T. DebRoy, “Heat and fluid flow in additive manufacturing – Part II: Powder bed fusion of stainless steel, and titanium, nickel and aluminum base alloys,” *Comput. Mater. Sci.*, vol. 150, no. April, pp. 369–380, 2018.

[28] T. Mukherjee, H. L. Wei, A. De, and T. DebRoy, “Heat and fluid flow in additive manufacturing—Part I: Modeling of powder bed fusion,” *Comput. Mater. Sci.*, vol. 150, no. April, pp. 304–313, 2018.

[29] C. Marangoni, “Uber die Ausbreitung der Tropfen einer Fluessigkeit auf der Oberflaesche einer anderen,” *Ann. Phys. Chem.*, vol. 143, no. 7, pp. 337–354, 1871.

[30] G. F. McLay, R., Carey, “Coupled Heat Transfer and Viscous Flow, and Magnetic Effects in Weld Pool Analysis,” *Int. J. Numer. Methods Fluids*, vol. 9, pp. 713–730, 1989.

[31] W. E. Khairallah, S.A., Anderson, A.T., Rubenchik, A., King, “Laser powder-bed fusion additive manufacturing: Physics of complex melt flow and formation mechanisms of pores, spatter, and denudation zones,” *Acta Mater.*, vol. 108, pp. 36–45, 2016.

[32] D. Dai and D. Gu, “Influence of thermodynamics within molten pool on migration and distribution state of reinforcement during selective laser melting of AlN/AlSi10Mg composites,” *Int. J. Mach. Tools Manuf.*, vol. 100, pp. 14–24, 2016.

[33] U. W. Zhang, O. Ridge, and O. Ridge, “Fluid Flow Phenomena during Welding[1],” *Weld. Fundam. Process.*, vol. 6, no. January, pp. 89–95, 2011.

[34] M. Tang, P. C. Pistorius, and J. L. Beuth, “Prediction of lack-of-fusion porosity for powder bed fusion,” *Addit. Manuf.*, vol. 14, pp. 39–48, 2017.

[35] J. L. Tang, M., Pistorius, P.C., Beuth, “Geometric model to predict porosity of part produced in powder bed system,” in *Materials Science and Technology*, 2015, pp. 129–135.

[36] D. Rosenthal, “Mathematical theory of heat distribution during welding and cutting,” *Weld. J.*, vol. 20, pp. 220–234, 1941.

[37] W. E. King *et al.*, “Observation of keyhole-mode laser melting in laser powder-bed fusion additive manufacturing,” *J. Mater. Process. Technol.*, 2014.

[38] J. Hann, D.B., Iammi, J., Folkes, “A simple methodology for predicting laser-weld properties from material and laser parameters,” *J. Phys. D Appl. Phys.*, vol. 44, p. 445401, 2011.

[39] H. E. Boulton, N.S., Lance-mmartin, “Residual Stresses in Arc Welded Plates,” *Proc. Inst. Mech. Eng.*, vol. 33, p. 295, 1986.

[40] R. Rosenthal, D., Schmerer, “Thermal Study of Arc Welding,” *Weld. J.*, vol. 17, no. 4, p. 2s, 1983.

[41] N. N. Rykalin, “Calculations of Thermal Processes in Welding,” 1951.

[42] K. Masubuchi, “Analysis of Welded Structures.” Pergamon Press, 1980.

[43] C. L. Tsai, “Parametric Study on Cooling Phenomena in Underwater Welding,” MIT, 1977.

[44] C. L. Tsai, “Finite Source Theory, Modeling of Casting and Welding Processes II,” in *Engineering Foundation Meeting*, 1983, p. 329.

[45] P. Myers, “Experimental and Computed Temperature Histories in Gas Tungsten Arc Welding in Thin Plates,” *Weld. J.*, vol. 48, no. 7, p. 295s, 1969.

[46] S. Kou, “3-Dimensional Heat Flow during Fusion Welding,” in *Proc. of Metallurgical Society of AIME*, pp. 129–138.

[47] P. G. Kogan, “The Temperature Field in the Weld Zone,” *Ave. Svarka*, vol. 4, no. 9, p. 8, 1979.

[48] M. A. Ecer, G.M., Downs, H.D>, Brody, H.D., Gokhale, “Heat Flow Simulation of Pulsed Current Gas Tungsten Arc Welding,” in *Engineering Foundation 1980 Meeting, Modeling of Casting and Welding Processes*, 1980, pp. 139–160.

[49] P. Hibbitt, H., Marcal, “A Numerical Thermomechanical Model for Welding and Subsequent Loading of a Fabricated Structure,” *Comput. Struct.*, vol. 3, p. 1145, 1973.

[50] E. Friedman, “Thermomechanical Analysis of the Welding Process Using Finite Element Methods.” Trans. ASME, p. 206, 1975.

[51] P. Paley, Z., Hibbett, “Computation of Temperature in Actual Weld Design,” *Weld. J.*, vol. 54, no. 11, p. 385s, 1975.

[52] T. Naka, “Temperature Distribution during Welding,” *J. Jpn. Weld. Soc.*, vol. 11, no. 1, p. 4, 1941.

[53] T. Masubuchi, K., Kusuda, “Temperature Distribution of Welded Plates,” *J. Jpn. Weld. Soc.*, vol. 22, no. 5, p. 14, 1953.

[54] C. A. Tsai, C.L., Hou, “Theoretical Analysis of Weld Pool Behavior in the Pulsed Current GTAW Process,” in *ASEM Winter Annual Meeting: Transport Phenomena in Materials Processing*, 1983.

[55] E. Friedman, “Finite Element Analysis of Arc Welding, Report WAPD-TM-1430,” 1980.

[56] Y. (Morris) Wang, C. Kamath, T. Voisin, and Z. Li, “A processing diagram for high-density Ti-6Al-4V by selective laser melting,” *Rapid Prototyp. J.*, vol. 24, no. 9, pp. 1469–1478, 2018.

[57] C. L. Tsai, U. S. Design, and U. S. Design, “Heat Flow in Fusion Welding[1],” *Weld. Fundam. Process.*, vol. 6, no. January, pp. 55–66, 2011.

[58] T. W. Eagar and N. S. Tsai, “Temperature fields produced by traveling distributed heat sources,” *Weld. J.*, vol. 62, no. 12, pp. 346–355, 1983.

[59] M. Lippold, J.C., Clark, W.A.T., Tumuluru, “An investigation of weld metal interfaces,” in *The Metal Science of Joining*, 1992, pp. 141–146.

[60] Z. Nie, P., Ojo, O.A., Li, “Numerical modeling of microstructure evolution during laser additive manufacturing of a nickel-based superalloy,” *Acta Mater.*, vol. 77, pp. 85–95, 2014.

[61] M. M. Parimi, L.L., A, R.G., Clark, D., Attallah, “Microstructural and texture

development in direct laser fabricated IN718," *Mater. Charact.*, vol. 89, pp. 102–111, 2014.

[62] M. T. Clark, D., Bache, M.R., Whittker, "Shaped metal deposition of a nickel alloy for aero engine applications," *J. Mater. Process. Technol.*, vol. 203, pp. 439–448, 2008.

[63] et al. Xiao, H., Li, S.M., Xiao, W.J., Li, Y.Q., Cha, L.M., Mazumder, J., "Effects of laser modes on Nb segregation and Laves phase formation during laser additive manufacturing of nickel-based superalloy," *Mater Lett*, vol. 188, pp. 260–262, 2017.

[64] M. Manikandan, S.G.K., Sivakumar, D., Rao, K.P., Kamaraj, "Effect of weld cooling rate on Laves phase formation in Inconel 718 fusion zone," *J. Mater. Process. Technol.*, vol. 214, no. 2, pp. 358–364, 2014.

[65] W. Rombouts, M., Maes, G., Mertens, M., Hendrix, "Laser metal deposition of Inconel 625: microstructure and mechanical properties.," *J Laser Appl*, vol. 24, no. 5, p. 052007, 2012.

[66] G. L. Dieter, G.E., Bacon, S.M., Copley, C., Wert, Wilkes, *Mechanical Metallurgy*. 1988.

[67] Z. . I. Yap, C.Y., Chua, C.K., Dong, "An effective analytical model of selective laser melting," *Virtual Phys. Prototyp.*, vol. 11, no. 1, 2016.

[68] C. Y. Yap, H. K. Tan, Z. Du, C. K. Chua, and Z. Dong, "Selective laser melting of nickel powder," *Rapid Prototyp. J.*, vol. 23, no. 4, pp. 750–757, 2017.

[69] I. Yadroitsev, I., Thivillon, L., Bertrand, P.H., Smurov, "Strategy of manufacturing components with designed internal structure by selective laser melting of metallic powder," *Appl. Surf. Sci.*, vol. 254, no. 4, pp. 980–983, 2007.

[70] Nanoval GmbH & Co, "NiNb Materials Safety Data Sheet." 2017.

[71] Y. Zhang, J. R. G. Evans, and S. Yang, “Corrected values for boiling points and enthalpies of vaporization of elements in handbooks,” *J. Chem. Eng. Data*, vol. 56, no. 2, pp. 328–337, 2011.

[72] P. N. Valencia, J.J., Quested, *Thermophysical Properties*. ASM Handbook, Vol. 15, 2008.

[73] M. W. Chase Jr., *NIST-JANAF Themochemical Tables, Fourth Edition*. 1998.

[74] C. D. Boley, S. C. Mitchell, A. M. Rubenchik, and S. S. Q. Wu, “Metal powder absorptivity: modeling and experiment,” *Appl. Opt.*, vol. 55, no. 23, p. 6496, 2016.

[75] M. Walker, J.M., Haberland, M., Taheri Andani, M., Karaca, H.E., Dean, D., Elahinia, “Process development and characterization of additively manufactured nickel-titanium shape memory parts,” *J. Intell. Mater. Syst. Struct.*, vol. 27, no. 19, pp. 2653–2660, 2014.

[76] J. Beuth and N. Klingbeil, “The role of process variables in laser-based direct metal solid freeform fabrication,” *Jom*, vol. 53, no. 9, pp. 36–39, 2001.

[77] T. Bormann, B. Müller, M. Schinhammer, A. Kessler, P. Thalmann, and M. De Wild, “Microstructure of selective laser melted nickel-titanium,” *Mater. Charact.*, vol. 94, pp. 189–202, 2014.

[78] T. Rai, R., Elmer, J.W., Palmer, T.A., Debroy, “Heat transfer and fluid flow during keyhole mode laser welding of tantalum, Ti-6Al-4V, 304L stainless steel and vanadium,” *Phys. D. Appl. Phys.*, vol. 40, no. 18, pp. 5753–5766, 2007.

[79] P. N. Valencia, J.J., Quested, “Thermalphysical Properties,” *ASM Handb.*, vol. 15, pp. 468–481, 2008.

[80] K. Abd-Elghany and D. L. Bourell, “Property evaluation of 304L stainless steel fabricated by selective laser melting,” *Rapid Prototyp. J.*, vol. 18, no. 5, pp. 420–428,

2012.

[81] A. International, *ASM Metals Handbook Vol. 2, Properties and Selection: Nonferrous Alloys and Special-Purpose Materials*. 1990.

[82] “Matweb, Material Property Data,” 2019. [Online]. Available: http://www.matweb.com/search/DataSheet.aspx?MatGUID=e6eb83327e534850a062dbca3bc758dc&ckck=1.

[83] M. W. Chase Jr, *NIST-JANAF Thermochemical Tables, Fourth Edition*. 1998.

APPENDIX

Excel Sheet for $NiNb_5$

Excel Sheet for New Material

1. Table of Contents Sheet

2. Material Properties and Process Parameters

Description of sheet

This sheet is where you input your material properties for the new material. The material properties are the inputs required for the Eagar-Tsai model. These include:

- Melting Temperature, T_m, [K]
- Thermal Conductivity, k, [W/(m-K)]
- Specific Heat Capacity, c, [J/(kg-K)]
- Absorptivity, ŋ, [0-1]
- Bulk Density, *p*, [kg/(m^3)]

Next to each value is where you can input a reference to where material property value came from or input the reasoning of how you calculated or estimated the value.

The next section is the lower and upper boundary conditions for the process parameters. The process parameters are:

- Laser Power, P, [W]
- Scan Speed, v, [mm/s]
- Layer Thickness, t, [µm]

- Hatch Distance, h, [µm]

This list can be extended if you choose to focus on other process parameters. Other important process parameters include beam spot size [µm] and scan strategy. Again, it is important to include your reasoning (or literature references) for choosing those lower and upper bound conditions.

The "Laser Power Calibration" section is the actual laser power out machine is outputting. [Note: this is for the 3D Systems ProX 200 PBF machine installed early 2018.]

Steps

1. Input material properties and include references/reasoning.

2. Input lower and upper bound conditions for process parameters. Include references and reasoning.

3. Eagar-Tsai Predictions for Single Track Experiments

Description of sheet

This sheet is where you perform a full factorial design of experiments on your new material using the Eagar-Tsai model to estimate the melt pool width and depth. Lack of fusion (LOF) can be predicted by making sure the melt pool depth is sufficient enough to melt the layer thickness or 1.5 times the layer thickness (t):

LOF occurs when $t / M_d > 1$ or more conservatively, when $1.5*t/M_d > 1$.

Since Eagar-Tsai cannot predict keyhole (KH) mode, we predict onset keyholing to occur when:

$KH = M_d \geq M_w/2$ or more conservatively, when $KH = M_d \geq M_w/2.5$.

Steps

1. Open online Eagar-Tsai Model Solver. Follow steps on each page. You can upload a text file with up to 12 runs. You can add a new material and its properties.

2. Run a full factorial design of experiments for the material under investigation.

3. Perform lack of fusion and keyhole mode calculations.

4. Pay attention to melt pool depth value (depending on layer thickness).

4. DOE for Single Tracks

Description of sheet

This sheet is a summary of the single track runs you want to perform experimentally.

Steps

1. Eliminate runs from the full factorial design on the previous sheet that would not be good candidates (but don't delete from previous sheet).

- Eliminate runs that have too low or too large of a M_d,
- Eliminate runs that have too low or too wide of a M_w, and
- Eliminate runs that are under the alloy's melting point or show significant boiling/evaporation.

Code for Temperature Field Data

The following code is for generating cross-section images of the melt pool in the XY and XZ planes. The code also determines the minimum and maximum temperatures within the melt pool. Code is written for MATLAB. The Online Eagar-Tsai Model Solver can only calculate the

temperature distribution for one P and v combination at a time. Simply copy and paste the url into the first line of code and change the title of the plots according to the P and v parameters tested.

```
//
url='http://54.234.147.81/downloads/try1_out.json';
value=jsondecode(urlread(url));
max(value.Tplanexy(:))
max(value.Tplanexz(:))
min(value.Tplanexy(:))
min(value.Tplanexz(:))
imagesc(value.Tplanexy)
hold on
contour(value.Tplanexy,'LevelList',1877,'color','k')
contour(value.Tplanexy,'LevelList',3315,'color','r')
title('Half Meltpool_XY Image for 20 W, 1 mm/s')
xlabel('Meltpool Length [µm]')
ylabel('Meltpool Width [µm]')
imagesc(value.Tplanexz)
hold on
contour(value.Tplanexz,'LevelList',1877,'color','k')
contour(value.Tplanexz,'LevelList',3315,'color','r')
title('Half Meltpool_XZ Image for 20 W, 1 mm/s')
xlabel('Meltpool Length [µm]')
```

ylabel('Meltpool Depth [μm]')

Melt pool image.m

Displaying Melt pool image.m.

//

2. Choose a minimum of 25 - 45 single track experiments to run. You want at least 25 - 45 runs to analyze data and calibrate in future steps.

5. Single Track Data

Description of sheet

This sheet collects all the melt pool width and melt pool depth data for each cross-section of the single tracks (bottom section of sheet). Keep this section organized and fill in the correct measurements with the correct cross-section. The average M_w and M_d as well as the standard deviation is calculated. A summary of the average widths and depths and the predicted values are in the top section of the sheet. Plot and compare the experimental and predicted values.

Steps

1. Measure and collect the M_w and M_d for 2 – 3 cross-sections per single track.

2. Calculate the average M_w and M_d and report in top section.

3. Compare the Eagar-Tsai Model predicted values to the experimental values. What conclusions can you make? Does the model overpredict, underpredict, or is it accurate? Is it more accurate in certain regions and inaccurate in others?

6. Cubes

Description of sheet

This sheet performs a DOE for cubes/pillars based off Eagar-Tsai and single-track experiments. The next section uses a simple MATLAB code to calculate the intersecting point of adjacent melt pools. The melt pool width and depth values from Sheet 5 can be input into the MATLAB code to achieve the appropriate geometry. Various hatch distances can be tested and the resulting t_{max} value can be analyzed to make sure it satisfies the layer thickness criteria.

Steps

1. After calibrating/adjusting the Eagar-Tsai model (using the surrogate model), determine what P and v parameters will produce sufficient melt pool depths for the layer thickness you are choosing to print with. (e.g., most prints are performed with a layer thickness of 30 µm).
2. Perform LOF calculations. Use MATLAB code to find maximum layer thickness for various hatch distance values. The maximum layer thickness should be able to satisfy layer thickness and melt pool depth conditions.
3. For the actual builds, choose a h value that is 80% of the optimal/maximum value to be conservative and ensure you will get a successful build.

Code for finding intersecting point for various hatch distances

```
clear all;
% Melt Pool 1 and Melt Pool 2 (melt pools are assumed to be ellipses)
%General equation when Mw > Md = '((x-h)^2)/Mw + y^2/Md = 1'
%General equation when Md > Mw = '((x-h)^2)/Md + y^2/Mw = 1'
```

```
%Optimize h value and look at value of intersecting point
%Value of intersecting point is maximum layer thickness
width = 129.57;
depth = 64.73;
hatch = 50;
syms x y
MeltPoolOne = ((x-0)^2)/(((width)/2)^2) + ((y+0)^2)/(((depth)^2));
MeltPoolTwo = ((x-hatch)^2)/(((width)/2)^2) + ((y+0)^2)/(((depth)^2));
MP_diff = [MeltPoolOne,MeltPoolTwo];
tmax = solve(MP_diff,[x y]);
% Find the points of intersection
X = double(tmax.x);
Y = double(tmax.y);
mask = ~any(imag(X), 2) | ~any(imag(Y), 2);
X = X(mask); Y = Y(mask);
disp([tmax]);
%plot
ezplot(MeltPoolOne, [-200, 300, -75, 0])
hold on
ezplot(MeltPoolTwo, [-200, 300, -75, 0])
%plot labels
% plot(X, Y, 'b.');
title('NiNb: P = 80 W, v= 50 mm/s, h = 35 um, tmax = 24.8 um');
```

```
xlabel('Melt Pool Width');
ylabel('Melt Pool Depth');
hold off;
```

7. Density & Porosity Data

Description of sheet

This sheet calculates the density and porosity of each cube using the Archimedes method.

Steps

1. Report values required for Archimedes method.

8. Vaporization Data

Description of sheet

This sheet collects all the data from the WDS experiments. Plots can be made to compare original nickel content (from powder) to the amount of nickel content lost for various parameter combinations.

Steps

1. Input WDS data of raw powder (composition of powder).
2. Input WDS data for each of the cubes (three locations: bottom, middle, and top of build).
3. Determine nickel content loss for each cube (three locations: bottom, middle, and top of build).
4. Plot nickel content loss as a function of power, speed, hatch distance, and VED.

9. Characterization

Description of sheet

This sheet includes links to zip files to SEM/BSE images of cubes.

X. Mechanical Testing Data

Description of sheet

This sheet includes the mechanical testing data (tension, compression, etc.).

Steps

1. Specify mechanical test (tension or compression) and other necessary information (e.g., strain rate, temperature, etc).

2. Collect sample number and failure analysis data.

3. Record ultimate tensile strength, yield strength, and ductility.

10. Build Time

Description of sheet

This sheet estimates how long it should take to build each cube and how long it should take to build "X" number of cubes.

Steps

1. Input your build dimensions.

2. Calculate the height (µm), base area (mm^2), and total number of layers:

    height of build / layer thickness.

3. Calculate the distance the laser travels:

base area / hatch spacing (µm).

Distance laser travels will be in *millimeters*.

4. Calculate how long it to build one layer:

distance laser travels / speed

5. Calculate how long it will take to build a single cube:

(time it takes to build one layer * total number of layers) / 60.

Answer is in *minutes*.

6. Now calculate the recoating time for each cube:

recoating time is 10 seconds per layer. Total recoating time is 10 * total number of layers.

7. Calculate the total time for each cube:

total time it takes to build the cubes + the total time it takes for recoating.

8. Calculate the total time for "X" number of cubes:

sum the total time it takes to build all cubes in experiment.

EXTRA SHEETS

11. Calibrated melt pool width and melt pool depth

Description of sheet

This sheet is not necessary for the process parameter selection guideline. However, before we had the surrogate model, this was what I used to record/test different NiNb material properties to adjust the melt pool width to align with the experimental values. I kept this sheet to show my work.

Steps

1. Record original material property values used for single track experiments.

2. We will be changing three material properties for the calibration: thermal conductivity, specific heat capacity, and absorptivity.

3. Change one material property at a time and determine melt pool dimension trend (increase or decreasing as property increases or decreases).

4. Change two material properties and record melt pool dimension outcomes.

5. Change three material properties and determine best values that match with experimental values.

12. Linear Energy Density & M_d

Description of sheet

This is an extra sheet used to test how various melt pool depths can be achieved with the same linear energy densities. Additional sheets can be used for plot data, analyze, etc.